https://doi.org/10.1016/j.addma.2024.104009

Strong yet ductile refractory high entropy alloy fabricated via additive manufacturing

Yongyun Zhang [1, 2], Bailiang Qin[1], Di, Ouyang[1,3], Lin Liu[3], Chuangshi Feng[2], Yuqiang Yan[2], Shulong Ye[4], Haibo Ke[2*], K.C. Chan [1*], Weihua Wang[2,5]

1. *Research Institute for Advanced Manufacturing, Department of Industrial and Systems Engineering, The Hong Kong Polytechnic University, Hong Kong, China.*
2. *Songshan Lake Materials Laboratory, Dongguan 523808, China*
3. *State Key Laboratory of Material Processing and Die & Mould Technology and School of Materials Science and Engineering, Huazhong University of Science and Technology, Wuhan, 430074, China*
4. *Faculty of Materials Science, Shenzhen MSU-BIT University, Shenzhen 518172, China*
5. *Institute of Physics, Chinese Academy of Sciences, Beijing 100190, China*

[*] Corresponding author.
E-mail address: (kehaibo@sslab.org.cn)

[*] Corresponding author.
E-mail address: (kc.chan@polyu.edu.hk)

Abstract

Refractory high-entropy alloys (RHEA), particularly those with a body-centered cubic lattice structure, are garnering increased interest due to their potential industrial applications. However, their strength-ductility trade-off at room temperature presents a challenge that requires resolution. In this study, we fabricated a ductile $Ti_{42}Hf_{21}Nb_{21}V_{16}$ RHEA for additive manufacturing using a directed energy deposition (DED) technique, with a focused laser serving as the energy source. The additively manufactured RHEA demonstrated an exceptional strength-ductility synergy, boasting a gigapascal yield strength and a substantial tensile strain until failure (~22.5%). Compared to its as-cast state, the tensile yield strength increased by 32 %, and ductility improved slightly by 2 %, suggesting a potential solution to the enduring strength-ductility trade-off dilemma. The enhanced yield strength can be attributed to solidification-enabled interstitial atoms resulting from the low-content nitrogen and oxygen atmosphere applied, while the high ductility is linked to the modified dislocation motion mechanism facilitated by the decomposition of the body-centered cubic matrix. This finding opens up possibilities for in-situ tailoring of microstructure and compositions to achieve superior mechanical performance in alloys through additive manufacturing processes.

Keywords: Refractory high-entropy alloys; additive manufacturing; improved strength-ductility synergy; interstitial atom strengthening; matrix decomposition.

1. Introduction

The concept of high entropy alloys (HEAs) [1,2] offers a limitless potential for designing alloys with exceptional properties based on the periodic table of elements. Refractory high entropy alloys (RHEAs), which consist of alloying constituents with higher melting points for maintaining their superior high-temperature properties [3], are being considered as potential candidates for the next generation of high-temperature alloys [4]. While many RHEAs exhibit ductility during compression tests at room temperature [5], only a small subset demonstrates acceptable tensile ductility, often at a sacrifice in yield strength [6], leading to the so-called strength-ductility trade-off [7]. So far, several studies have shown promising results in improving strength while preserving ductility in RHEAs, such as introducing local chemical fluctuations [8], forming oxygen complexes [9], creating spinodal modulations [6], or employing metastability engineering [10] to enhance their mechanical performance, especially their plasticity. However, additional machining is still necessary to produce final parts with complex shapes to meet specific application requirements [11].

Facing the long-standing challenge of balancing strength and ductility, additive manufacturing (AM) technology offers a promising solution by introducing unique heterogeneous structures [12] or dislocation structures [11] etc. Laser-aid AM processes are commonly used for fabricating metallic materials, such as Ti alloys [13,14], HEAs [15] and so on, via layer-by-layer production from digital files, allowing for highly customized production and freedom of design [16]. Although promising,

these strengthened alloys often sacrifice ductility compared to those as-cast counterparts, especially in HEAs with face center cubic (FCC) structure [17]. Compared to the widely used casting methods for RHEAs, AM approaches have the potential to eliminate coarse grains and macro-scale segregation due to higher cooling rates [18,19]. The directed energy deposition (DED) approach, specifically the use of focused laser in laser-engineered net shaping (LENS), is more suitable for fabricating RHEAs using pre-mixed [20,21] or high-throughput mixed elemental powders [22,23]. However, challenges remain in fabricating RHEAs via the LENS process, such as the presence of un-melted powders [20,23,24] and cracks [18,23,25], leading to passable strength but poor ductility. The former issue can be addressed by applying a remelting procedure [20], but the latter remains a challenge in achieving the desired mechanical properties of RHEAs via LENS. To address this issue, alloying regulation, like increasing the Nb content in specific RHEA systems, can improve the inherent fracture toughness [23] or hinder the formation of the pernicious ω phase to mechanical properties (so-called phase engineering)[21]. While the high-throughput metallurgical alloying [22,23,26] can guide the design of RHEAs, like crack-free TiZrHfNbTa RHEA by LENS [26], their compressive ductility is not as competitive as that of as-cast counterparts [27]. Due to the limited formation dimensions, the evaluation of the compressive properties is mainstream for RHEAs fabricated via LENS, while tensile properties are more suitable for assessing their potential in engineering applications [21]. So far, only a few attempts have been made to assess the tensile mechanical properties of HfNbTiZr RHEA fabricated via LENS [21], still highlighting the need to

address the strength-ductility trade-off and fully understand the enhanced mechanism in RHEAs fabricated via additive manufacturing compared to the as-cast counterpart [9].

In this study, we focused on the $Ti_{42}Hf_{21}Nb_{21}V_{16}$ RHEA system as our model alloy, exhibiting excellent ductility and possessing the decomposed phase structure after a complex thermal-stress environment following the LENS procedure, resulting in impressive mechanical performance. By maintaining a low content of oxygen and nitrogen atmosphere during the LENS procedure, the fabricated RHEA is strengthened by the solid soluble interstitial atoms, as opposed to the typical strengthening effect induced by dislocation networks in FCC-based alloys. Additionally, the triggered matrix decomposition that occurs during complex thermal-stress procedures contributes to a prolonged fracture strain compared to the as-cast counterpart. Overall, our findings propose a solution to the strength-ductility trade-off dilemma in RHEAs, guiding the design of refractory alloys that are both strong and ductile and opening up the possibility of directly manufacturing RHEA products in the future.

2. Materials and Methods

2.1 Materials and alloy fabrication

2.1.1 Raw powders

The feedstock powders used for RHEA fabrication include plasma rotation electrode atomized spherical titanium (Ti, purity> 99.95%), niobium (Ti, purity> 99.95%), hafnium (Hf, purity> 99.95%) and vanadium (V, purity> 99.95%) powders，ranging in size from 50 μm to 100 μm (D_{50}=75 μm), as shown in **Fig. 1**. The powders

exhibit a perfect spherical shape (**Fig. 1a**), indicating good flowability. Initially, the powders were blended in a powder mixer (Turbula, T2F) at room temperature for 2 h, with a revolving speed of 200r/min, within a sealed container.

2.1.2 LENS fabrication process

The bulk RHEA sample of size 12 × 70 × 4 mm was fabricated on a pure Ti substrate by additive manufacturing in the form of LENS (Optomec LENS MR-7), schematically illustrated in **Fig. 1b**. The LENS MR-7 is a coaxial powder feeding 3D printer that utilizes a high-powered laser system within a closed chamber filled with argon. The laser, with a spot size of ~ 600 μm, was used to form the melt pool and remelt the previous path. It is common to encounter un-melted powders when fabricating RHEAs via laser deposition by blended elemental powder, due to the difference in melting points [20,23,24]. To ensure a uniform elemental distribution, a remelting procedure was employed in our study, as schematically shown in **Fig. 1c.**

The scanning strategy for the fabrication process is as follows,

1) Layer building: The first layer was scanned in a zigzag strategy, with a powder feed rate of 4g/min and a laser power of 550 W;

2) Remelting procedure: After the first laser stopped, the powder delivery nozzle moved upward by 200 μm (offset value) and the remelting process began. The procedure involved a 45 °rotation compared to the previous layer. No powder was delivered to the molten pool during this step and the laser power was increased to 800 W;

3) Layer building: Once the remelting process was completed, the powder delivery nozzle was immediately raised by 200 μm, and the powder feed rate was initiated. The working laser power was set to 550 W, and a 45 °rotation was applied for layer building;

4) Remelting procedure: A scan rotation of 45 °, compared to the previous layer, was applied, and a similar remelting procedure (2) was applied to remelt the previously built layer.

The four steps were repeated periodically until a bulk specimen with a thickness of ~ 4 mm was built. The other parameters used in this study remained constant, including a working distance of 10 mm, a scanning speed of 5 mm/s, and a hatching space of 381 μm. Before the experiment, flowing argon was used to reduce the oxygen level to ~ 200 ppm in the atmospheric chamber which was maintained throughout the entire printing process. After a whole procedure, the actual composition of LENS-fabricated RHEA was determined by energy disperse spectroscopy (EDS).

2.1.3 Other fabrication procedures

For comparison purposes, we applied the other fabrication procedures to manufacture the reference samples, including the post-heat treatment and casting RHEA with the same elemental compositions. Due to the application of high remelting laser power during the fabrication of the LENS-fabricated sample, severe residual stress was produced. To mitigate this stress and enhance the mechanical performance of the LENS-fabricated sample, a vacuum annealing approach was employed, referred to as-

HT state. The annealing process involved heating the samples to 1273 K for 4 hours, with a heating rate of 10 K/min and subsequent furnace cooling (**Fig. 1d**).

Reference samples with the same composition (obtained via EDS) were fabricated using pure Hf, Nb, Ti and V nuggets (with a purity of 99.99%) through arc melting and water-cooled copper-mould casting (referred the as-cast state). The pre-cleaned nuggets were placed top-down with decreased melting points for each element nugget in the copper cavity. The furnace chamber was evacuated to 5×10^{-3} Pa and then filled with argon to 0.5 Pa, a process repeated three times to ensure minimal oxygen content in the working chamber. The base materials were melted and remelted ten times to ensure an even distribution of alloying elements in the as-cast sample. Finally, the molten ingot was air-soaked and solidified into a water-cooled copper mould cavity with dimensions of $10\times5\times120$ mm.

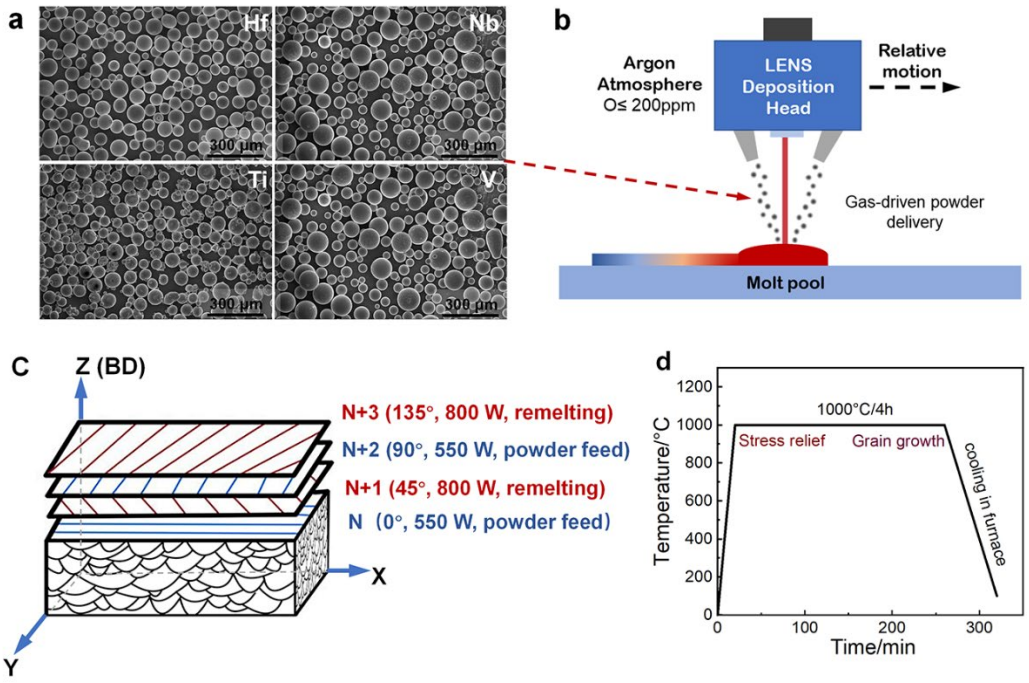

Fig. 1 The materials and experimental design. a, SEM morphologies of raw elemental powders (Hf, Nb, Ti and V) used in **b,** LENS with its schematic diagram. **c,** gives the fabrication strategy during the LENS procedure and **d,** exhibits the heat treatment procedures on the LENS-fabricated samples.

2.2 Composition identification

As the composition offset generally formed in the LENS-fabricated alloys prepared by mixed pure elemental powders with the nominal compositions [28–30], we conducted the EDS tests on the LENS-fabricated RHEA as well as its heat-treated one to determine their actual compositions after LENS. Moreover, we dispense the antithetical RHEA through casting by referring to the actual composition in the LENS-fabricated sample, whose results are listed in **Table 1**. Considering the absorption of oxygen and nitrogen in Ti-based alloys under high temperatures [31], we also conducted the precise oxygen and nitrogen determination by the ON836 Oxygen/Nitrogen system (LECO, USA) with the ultra-precision of 0.025 ppm under the Ti-based method. The pre-weighted RHEAs (~ 200 mg) fabricated through different

approaches were placed in the graphite crucible and then melted to release analyte gases. The detected oxygen and nitrogen content in those RHEAs is also listed in **Table 1**. Based on the EDS results, the LENS-fabricated RHEA has an atomic ratio of Ti:Hf:Nb:V=42:21:21:16. As a result, the fabricated RHEA is referred to $Ti_{42}Hf_{21}Nb_{21}V_{16}$ RHEA, and we also prepared the as-cast counterpart with same composition for comparison.

Table 1 The nominal and EDS-obtained elemental compositions of the investigated RHEAs and their oxygen and nitrogen contents obtained through an Oxygen/Nitrogen detector.

Element	Ti	Hf	Nb	V	O	N
	at.%					
Nominal composition	38	24	23	15	-	-
As-cast	41.89	21.17	21.15	15.79	0.007 (13 ppm)	0.018 (29 ppm)
As-LENS	41.71	21.33	20.90	16.06	0.028 (52 ppm)	0.111 (185 ppm)
As-HT	41.77	21.25	21.23	15.75	0.029 (54 ppm)	0.107(179 ppm)

2.3 Calculations

2.3.1 Calculation of the Phases Diagrams (CALPHAD) approach

The ThermoCalc software with the newly developed TEHEA thermodynamic database was used to calculate the phase formation, phase composition and other parameters for the specific alloy system. It provided reliable thermodynamic parameters for studying HEAs. In this study, we used the ThermoCalc software not

only to study the equilibrium calculation in our RHEA system but also to use the Scheil simulation to predict the phase formation during the rapid quenching in the LENS process.

2.3.2 DFT calculations

In this work, the lattice constant and elasticity of the RHEA were calculated using the virtual crystal approximation (VCA) based on the Cambridge Sequential Total Energy Package (CASTEP) [32]. The Perdew-Burke-Ernzerhof (PBE) in the generalized gradient approximation (GGA) Exchange-Correlation functional was used in the CASTEP package, with the TPSD algorithm chosen for the geometric optimization of the structure. The OTFG norm serving pseudopotential was selected with a customed cutoff energy of 1200 eV and k-points of 5 × 4 × 1. In the MonkhorstPack scheme, the Brillouin zone was sampled with the maximum total energy loss of 1×10^{-5} eV • $atom^{-1}$. The forces on a single atom converged to lower than 0.03 eV • $Å^{-1}$, while the maximum atom placement was less than 0.001Å and the total stress tensor order was reduced to 0.05 GPa.

2.4 Microstructural characterization

To characterize the phase structure of the samples, X-ray diffraction (XRD, Rigaku, Smartlab) was conducted with copper radiation by setting a step size of 1 °/min and 2θ ranging between 20 to 110 degrees. The microstructure was examined using a scanning electron microscope (SEM, ThermoFisher, Verios 5UC) equipped with an EDS system (Oxford Inc., X-max 80) to study the elemental distribution in RHEA

samples. An electron backscattered diffraction (EBSD, Oxford Inc., C-swift) experiment was conducted on a SEM (ThermoFisher, Verios 5UC) to investigate the metallurgical microstructure as well as phase compositions in the RHEA samples fabricated using different methods. For the EBSD sample preparation, the RHEA samples were electrical-wire-cutting from the base metal and then ground. Subsequently, they were polished until there were no obvious scratches. To eliminate superficial stress which would affect the confidence factor of EBSD results, flat Ar-ion beam milling (Leica, EM TIC 3X) was applied, at a working voltage of 5.5 kV for 40 min. The magnification was kept at 200X for the un-deformed samples with a step size of 1.5 μm, while it was 500X and 500 nm respectively for the deformed specimens. The working voltage in SEM was maintained at 30 kV during the EBSD procedure. The collected EBSD results were analyzed using Aztec Crystal software (Oxford Inc.) The microstructure of the different samples, either the deformed or the originally stated, was observed in a SEM (ThermoFisher, Verios 5UC) in the backscattered electron (BSE) mode, while the fracture morphology analysis was performed in the secondary electron (SE) mode. The transmission electron microscope (TEM) observations were conducted on samples prepared differently: the original RHEAs were prepared by the Ar-ion milling (PIPS II 695c) on a ~30 μm thick disc with a diameter of 3 mm, while the deformed microstructure specimen was prepared via focused ion beam (FIB, ThermoFisher, Helios 5UX). The further microstructures at an atomic level were revealed on TEM (ThermoFisher, Talos F200X) operated at 200 kV as well as an aberration-corrected TEM (ThermoFisher, Spectra 300) equipped with a high angle

annular dark field (HAADF) and EDS (Super-X) detectors. To perform in-situ tensile testing on the LENS-fabricated sample, a dual-tilt straining holder was utilized in the Talos F200X TEM operated at 200 kV. The tensile specimen, in a dog-bone shape, was prepared via Helios 5UX FIB, with a dog-bone shape and loaded to a TEM in-situ force-heat coupling test system (INSTEMS-MT, Bestron, China), given in **Fig. 2**a. The in-situ tensile specimen was sampling from the region in **Fig. 2**b, with the preferred orientation of <0 0 1> illustrate by **Fig. 2**c.

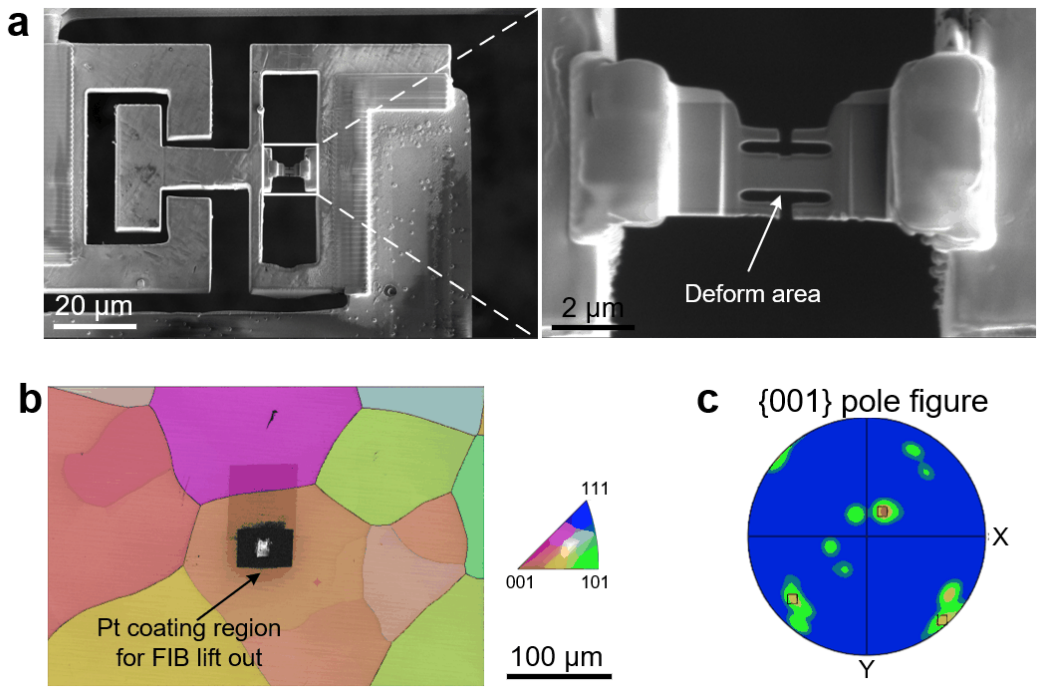

Fig. 2 The in-situ TEM tensile test sample preparation. a, tensile bar equipped on the MEMS chip on the in-situ force-heat coupling test system fabricated via FIB lift-out method from the **b,** marked region in EBSD IPF figure with **c,** corresponding {001} pole figure of the target region.

2.5 Measurement of properties

The tensile specimens were prepared from the as-cast, LENS-fabricated and as-HT samples in a dog-bone-like shape. The room-temperature tensile properties were determined using a universal testing facility (ZwickRoell, Proline) equipped with a digital image correlation (DIC, ZwickRoell) system with a strain rate of 1×10^{-3}/s. We calculated the local strain evolution profiles during the tensile tests via the testXpert III software (ZwickRoell) to determine the onset of necking of the RHEAs fabricated though different approaches. The tensile bars were machined in the horizontal direction with a gauge dimension of $6 \times 2 \times 1$ mm^3. Three samples were measured to obtain the average mechanical properties. After the tensile test, the microstructure on the top surfaces after deformation was observed using SEM and EBSD. The in-situ tensile experiment was conducted in TEM (ThermoFisher, Talos F200X), on the LENS-fabricated sample obtained FIB (ThermoFisher, Helios 5UX) to study the dislocation evolutions during the deformation.

3. Results

3.1 Calculation results

The LENS process involves high cooling rates (~10^3 – 10^4K/s [33]), which deviates the microstructure from the equilibrium calculations. The Scheil solidification process simulations can be performed in ThermoCalc software based on the assumptions of liquid-solid interface equilibrium, infinite diffusion in the liquid and no diffusion in the solid. This allowed us to predict the as-solidified microstructures in

RHEAs prepared via the LENS method. The equilibrium and no-equilibrium phase diagrams are given in Fig. 3 a and b, respectively, indicating that a single bcc-structure phase would be formed after the LENS procedure based on the given compositions.

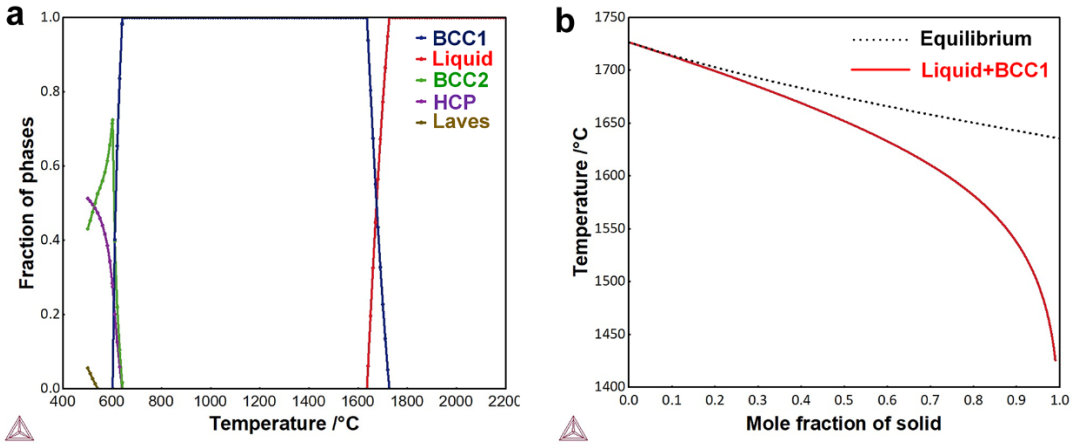

Fig. 3 The CALPHAD calculation results of the fabricated RHEA system. a, Fraction of phases as a function of temperature. **b,** Scheil diagram

Before the calculation of the lattice constant, we ensured the convergence parameters until the error on the calculated total energy reached the criteria of 0.001 ev/atom [34]. We used the VCA method to study the lattice constant of $Ti_{42}Hf_{21}Nb_{21}V_{16}$ RHEA, which was calculated to be 3.318 Å, with an error of less than 1% compared to the experimental result of as-cast sample (given in Section 3.2). This indicates that the parameter setting in this calculation procedure was reasonable. By establishing the relationship between the unstable stacking fault energy (USFE) and surface energy (SE), the intrinsic embrittlement or ductility can be reflected through these mentioned parameters (details can be found in Section 4.1). **Fig. 4**a illustrates a supercell consisting of 13 atomic layers with an ABABABABABABA stacking sequence of the closed-

packed (110) plane, with a vacuum layer of 15 Å. The formation of an unstable stacking fault (USF) at the shear direction of the upper part along [111] at the step of 0.1 is also shown. The GSFE can be obtained based on the following equation [35]:

$$\gamma_{SFE} = \frac{1}{A}(E_u - E_0) \qquad \text{Eq. 1}$$

where A is the stacking fault area, E_u and E_0 denote the total energy of the supercell with and without a shear displacement, respectively. After the calculation, we obtained the GSFE curve, (see **Fig. 4**b), with the USFE of 313.9 mJ/m2.

For the s unrelaxed surface energy calculation, the divided two parts underwent the compressive and tensile calculations (see **Fig. 4**c) with a step of 0.1 Å to fit the energy *vs* displacement curve to obtain the free surface energy of (110) lattice plane using the universal binding-energy relation (UBER) method, describing as follows [36]:

$$E_x = -\gamma_S \left(1 + \frac{x}{l}\right) e^{-\frac{x}{l}} + C \qquad \text{Eq. 2}$$

where γ is the unrelaxed (110) surface energy, l is a scaling length and C is a constant in this equation. Thus, based on the change in total energy E_x with displacement obtained by calculation results, plotted in **Fig. 4**d, yielding the surface energy value of 3190 mJ/m^2 in the target RHEA.

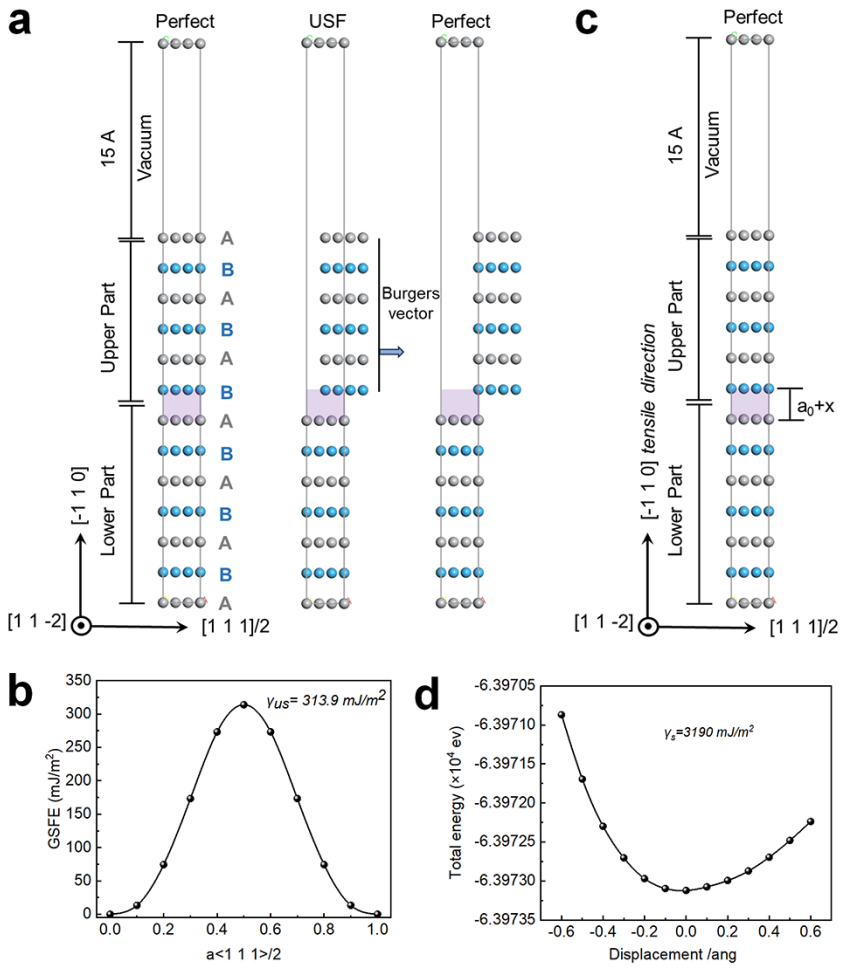

Fig. 4 DFT calculations on $Ti_{42}Hf_{21}Nb_{21}V_{16}$ RHEA. a, The BCC supercell containing the atomic stacking. **b**, First-principle calculated GSFE curves of targeted RHEA system. **c**, The BCC supercell is used for tensile and compression DFT calculations. **d**, The fitted total energy versus displacement curve via the UBER method.

3.2 Microstructure of fabricated RHEAs

In our study, we examined the microstructures of RHEA specimens fabricated using different methods: casting (as-casting), LENS (as-LENS) and LENS-fabricated RHEA followed by heat treatment (as-HT). The microstructure collected from the top surface revealed that the LENS-fabricated RHEA exhibited an equiaxed grain morphology (**Fig. 5a**), and its corresponding elemental mapping results (**Fig. 5b**)

demonstrated an even distribution of alloying elements, indicating the absence of macro-elemental segregations and un-melted powders when employing a higher laser powder remelting approach. The EBSD IPF figures collected form the XY and XZ planes (see **Fig. 1c**) are given in **Fig. 5a** showing that the LENS-fabricated $Ti_{42}Hf_{21}Nb_{21}V_{16}$ RHEA has a columnar grain morphology along the building direction (BD) and the equiaxed grain on the top surface (**Fig. 5a**). This difference in grain morphology is attributed to the higher ratio between the temperature gradient in solid/liquid interface (G), which can increased to 10^3 K/mm in the additive manufacturing process [21], and solidification velocity (R) [37,38], differing from the equiaxed grains formed in LMD-fabricated HfNbTiZr RHEA [21].

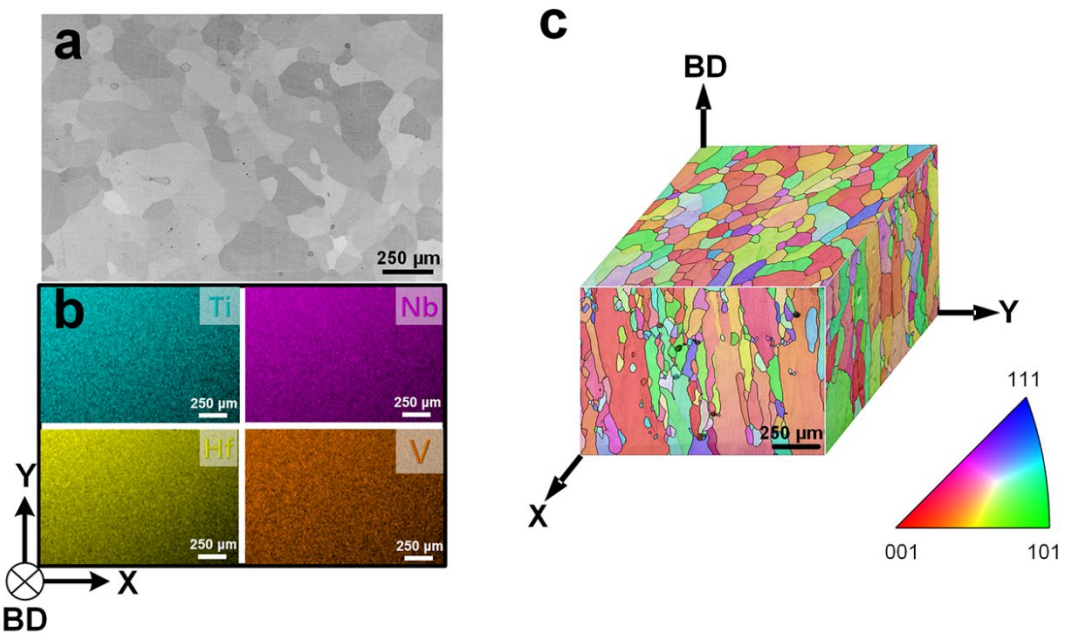

Fig. 5 The microstructure of LENS-fabricated RHEA. a, The BSE image from the as-LENS specimen. **b,** Corresponding EDS mapping. **c,** a 3-dimensional reconstructed EBSD structure showing the presence of columnar grain growth along the BD.

Further analysis of the microstructure of different RHEAs fabricated using several approaches was studied as follows. The EBSD IPF maps (**Fig. 6**a) collected on the top surfaces of tensile bars from RHEAs reveal the formation of equiaxed grains, whereas the grain size and preferable orientations vary among those samples. The LENS-fabricated sample exhibits the smallest grain size of 196 μm, while the grain sizes of the other samples are at the same level of ~ 240 μm (as shown in the statistical chart in **Fig. 6b**). The kernel average misorientation (KAM) figures (**Fig. 6c**), which can be used to assess the geometrically necessary dislocation densities [39] and the dislocation structures [40], revealed no significant difference in their densities among the RHEAs fabricated using different approaches. This is in contrast to the unique dislocation

networks typically formed in the FCC alloys [11,41] fabricated via the additive manufacturing method. The pole and inverse pole figures derived from the top surface of LENS-fabricated samples (**Fig. 6**d) illustrate the presence of <001>/(110) texture in the as-LENS RHEA with a preferable growth orientation of <0 0 1> parallel to the BD. Conversely, the pole figures of the as-cast $Ti_{42}Hf_{21}Nb_{21}V_{16}$ RHEA (**Fig. 6**e) indicate the absence of any noticeable obvious texture, while long-time high-temperature annealing primarily promoted grain growth rather than altering its preferable orientation.

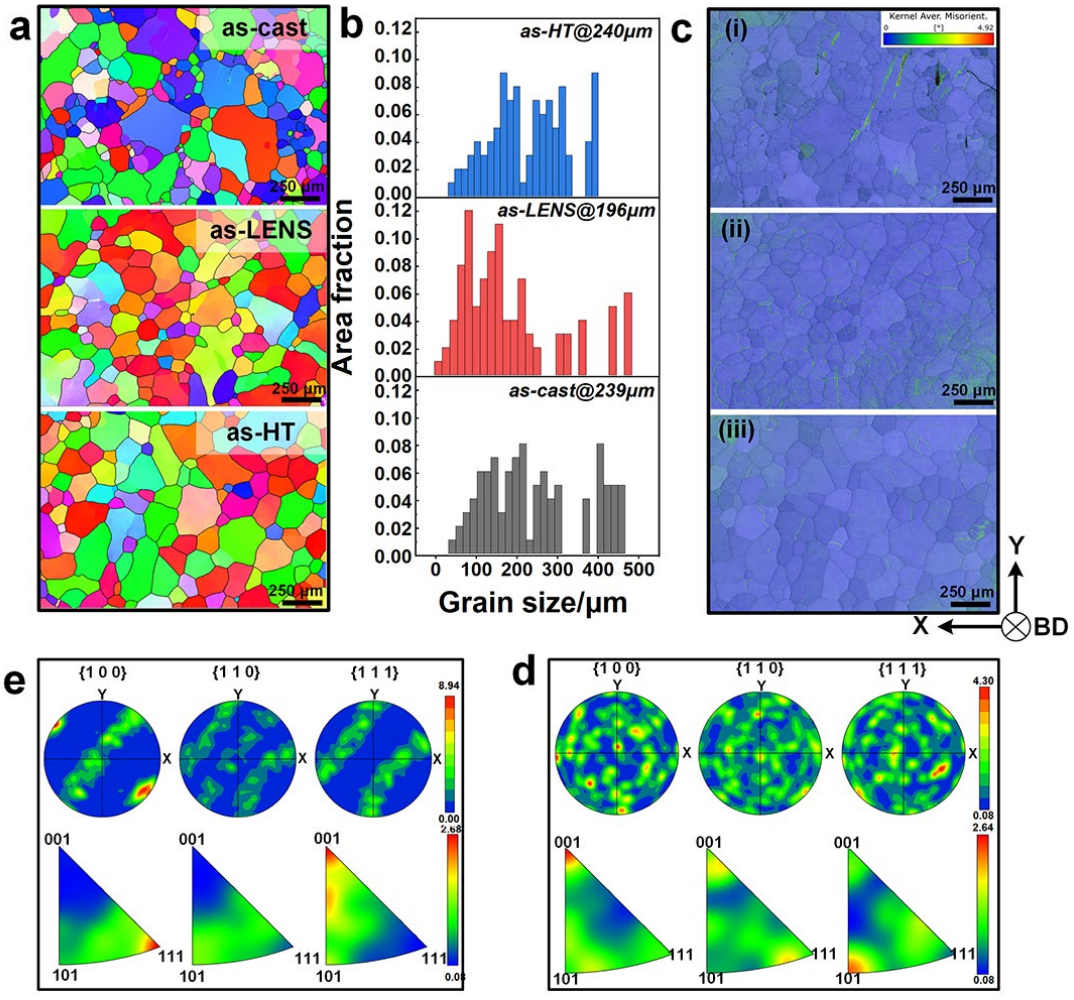

Fig. 6 The microstructural characterization of $Ti_{42}Hf_{21}Nb_{21}V_{16}$ RHEAs prepared via different approaches. a, The EBSD IPF maps from RHEAs fabricated using different

approaches with corresponding statistics of grain size distribution given in **b. c**, KAM maps giving that no dislocation networks formed in RHEAs fabricated after LENS. **d,** The collected pole figures and inverse pole figures from the top surface of as-LENS RHEA. **e**, The pole figures and inverse pole figures of as-cast RHEA.

The CALPHAD method demonstrates that the target system can produce a single BCC structure in the non-equilibrium cooling processes (**Fig. 3**). Additionally, EBSD phase maps (**Fig. 7a (i-iii))** indicate that there seem to be single BCC structures among those RHEAs. However, the XRD profile (**Fig. 7b**) reveals the formation of a single BCC phase in the as-cast specimen with a lattice constant of ~ 3.325 Å. Conversely, the as-HT RHEA exhibits diffraction peak splitting of the (310) crystal plane, similar to HfNbTiV RHEA [6], suggesting the separation of the BCC matrix into the primary phase of β_1 and the secondary separated phase of β_2. The lattice constant of the BCC matrix in the as-LENS and as-HT RHEAs is larger, approximately 3.330 Å, compared to the as-cast sample, due to the solid soluble interstitial atoms in the RHEA matrix [42].

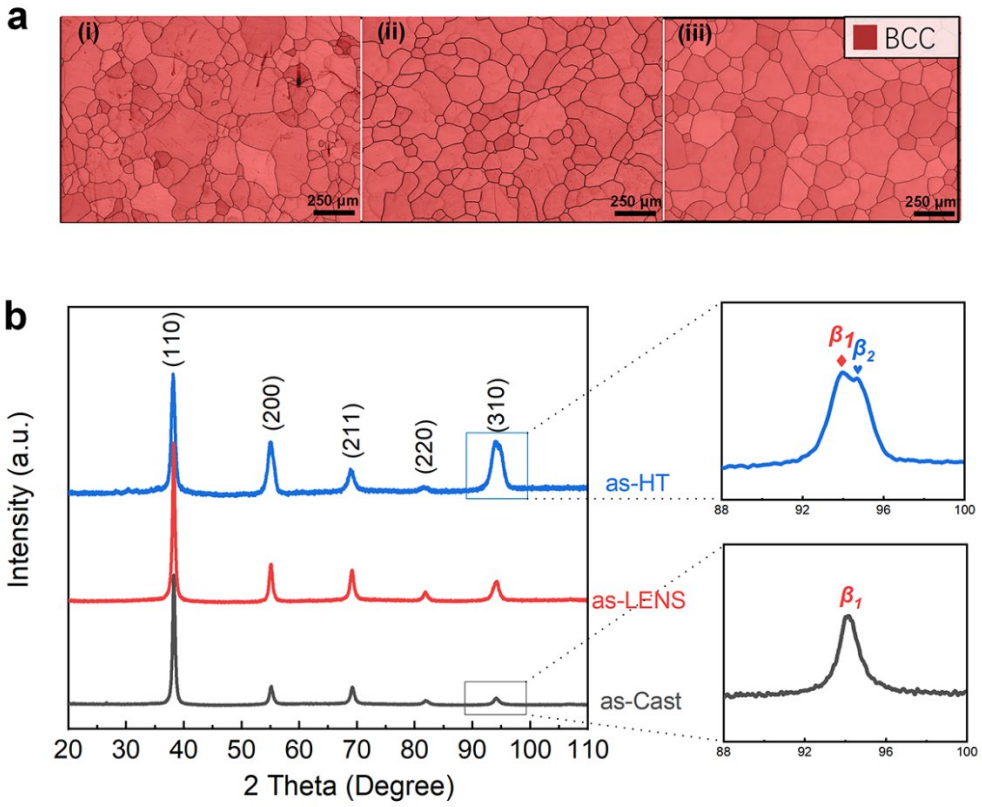

Fig. 7 Phase identification of $Ti_{42}Hf_{21}Nb_{21}V_{16}$ RHEAs prepared via different approaches. a, The EBSD phase maps. **b**, The XRD profiles of RHEAs fabricated using varied methods.

The TEM observation in **Fig. 8a** illustrates that the nano-scale phase separation occurs not only in as-HT RHEAs (**Fig. 8a** (iii)) but also in the as-LENS one, despite the selected area electron diffraction (SAED) patterns showing the characteristic of a single BCC phase in the inserts of **Fig. 8a**. To confirm the presence of phase separation in the as-LENS RHEA (**Fig. 8b**), the atomic-scale characterization and the corresponding Fast Fourier Transformation (FFT) images ((ii-iii)) of the marked area are given in **Fig. 8b** (i), revealing a structure different from the BCC matrix. A distinct interface between the BCC matrix and separated phase was characterized as given in **Fig. 8c** (i), with the corresponding FFT images showing an even more obvious BCC matrix separation after

heat treatment. Although the spinodal modulations were observed in the equimolar HfNbTiV RHEA [6], the separated structure would not be a secondary BCC structure due to the distortion of the SAED patterns between **Fig. 8b** (ii) and (iii). Based on the FFT patterns compared with simulated ones via the CrysTBox package [43] and XRD profile, a contracted body-centered tetragonal (BCT) structure (similar to the structure in $Ti_{38}V_{15}Nb_{23}Hf_{24}$ RHEA [44]), with the lattice parameters of a=c=3.330 Å and b=3.315 Å, was formed in the as-LENS sample and promoted by high-temperature annealing. Significant atomic distortion (x and y directions) obtained via geometrical phase analysis (GPA) [45] occurs at the interface between the separated phases (**Fig. 8c** (iii-iv)), consequentially resulting in the complex interaction with dislocation that would modify the deformation process in those RHEAs. The presence of Hf atoms with a relatively larger atomic radius induces a larger lattice distortion [46] leading to the lattice strain and higher strength in the HEAs compared to the conventional alloys [47]. The atomic EDS mapping collected from the as-LENS RHEA shows the nano-scale chemical heterogeneity (see **Fig. 8d**) and the formation of elemental rich clusters pointing by the green and white arrows, regardless of the manufacturing approaches, which can contribute to the ductility increase instead of strengthening RHEA [21].

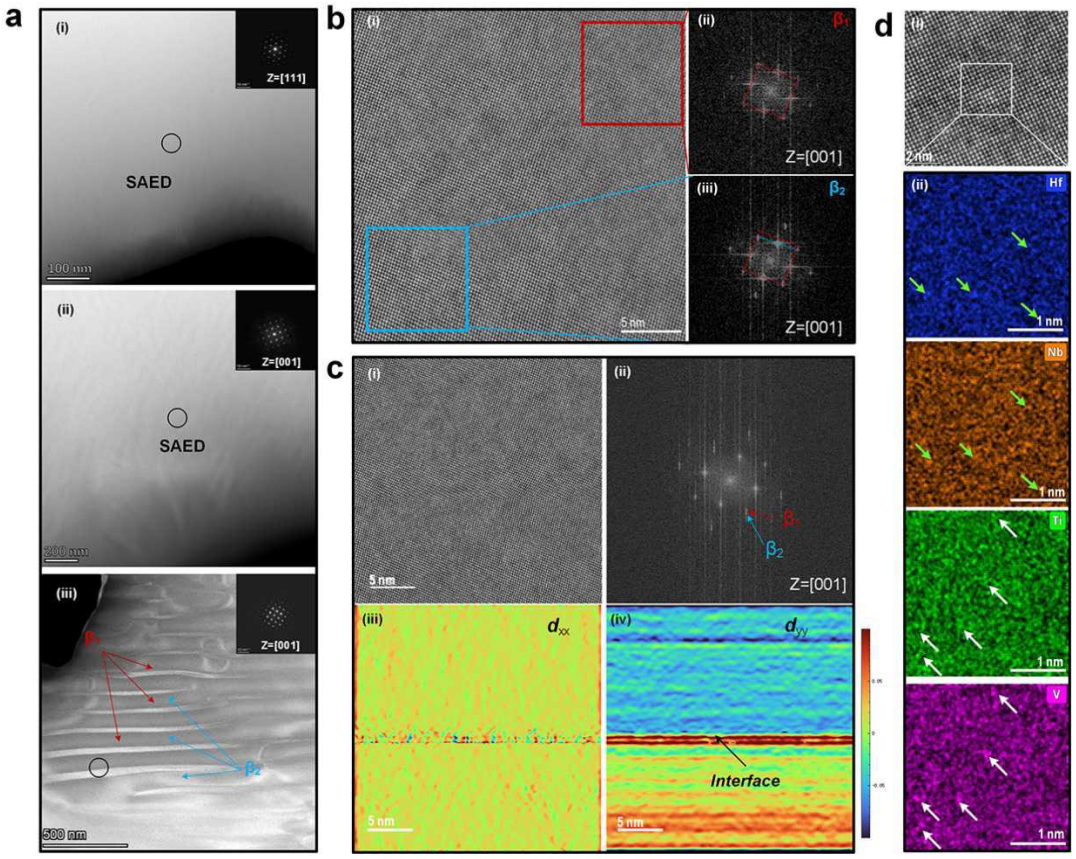

Fig. 8 Nano-scale microstructure of RHEAs fabricated via different approaches. a (i-iii) bright field TEM images collected from RHEAs prepared via casting, LENS as well as-HT with the SEAD patterns insert. **b**, The HRTEM figure with the corresponding FFT figures (**ii** and **iii**) from the as-LENS sample. **c(i)**, The HRTEM figure collected from the as-HT sample shows a clear interface of separated phases illustrated by (**ii**) the corresponding FFT image and (iii-iv) gives atomic distortions near the interface. **d(i)**, The HRTEM image with (**ii**) corresponding atomic scale EDS mapping. TEM figures are collected along the [001] zone axis.

3.3 Improved tensile strength-ductility synergy

We performed room temperature tensile tests on the RHEA specimens fabricated using different methods, and the results are presented in **Fig. 9**. Among these samples, the LENS-fabricated sample shows the best strength-ductility combination (see **Fig. 9a**) with a yield strength of 1034 MPa and fracture strain of 22.5 %. In comparison, the as-cast RHEA has a yield strength of 780 MPa and fracture strain of 20.2 %. The results

indicate that LENS fabrication can significantly increase the yield strength (by almost 32%) without compromising ductility, effectively overcoming the strength-ductility trade-off in specific RHEAs. It is worth noting that, after high-temperature annealing of the LENS-fabricated samples, the yield strength and the fracture strain were both slightly decreased to 970 MPa and 21.6 %, respectively. Additionally, we also converted the slope of the true stress-strain curve into the strain-hardening rate (SHR) curves, as shown in **Fig. 9b**, showing the plummet (Stage I), steady increase (Stage II) and then decreased trends (Stage III) on the plastic flow. During the deformation Stage I, a sharp drop in SHR is formed, while a gradual decrease in SHR also occurs in the deformation stage III. The plastic deformation stage II, characterized by a slight increase in SHR, terminates at different true strains of RHEAs fabricated via different approaches. Insert of **Fig. 9b** reveals the local strain profiles by DIC at the last frame before fracture collected along lines in **Fig. 11 a** and also displays the necking onsets, giving that the as-cast RHEA has the longest necking length while the as-HT counterpart has the shortest one (details are giving as follows). For comparison, we included Ashby plots of Ti-based alloys fabricated using additive manufacturing processes [14], the as-cast RHEAs [4], the previously reported LMD-fabricated HfTiZrNb RHEA [21], and our results (see **Fig. 9c)**. Our $Ti_{42}Hf_{21}Nb_{21}V_{16}$ RHEA fabricated using LENS stands out and has a superb strength-ductility synergy as well as specific yield strength-strain matching among the reported well-performed RHEAs (see **Fig. 9d**) [6]. Only a few others, such as equimolar HfNbTiV [6], and oxygen-doped HfNbTiZr RHEAs [9] can succeed in this RHEA, attributed to the presence of the spinodal structure as well as the oxygen

complex. However, their SHRs plunge to under true stress at the early plastic deformation [6], yet they still exhibit superior strength-ductility synergies in those RHEAs.

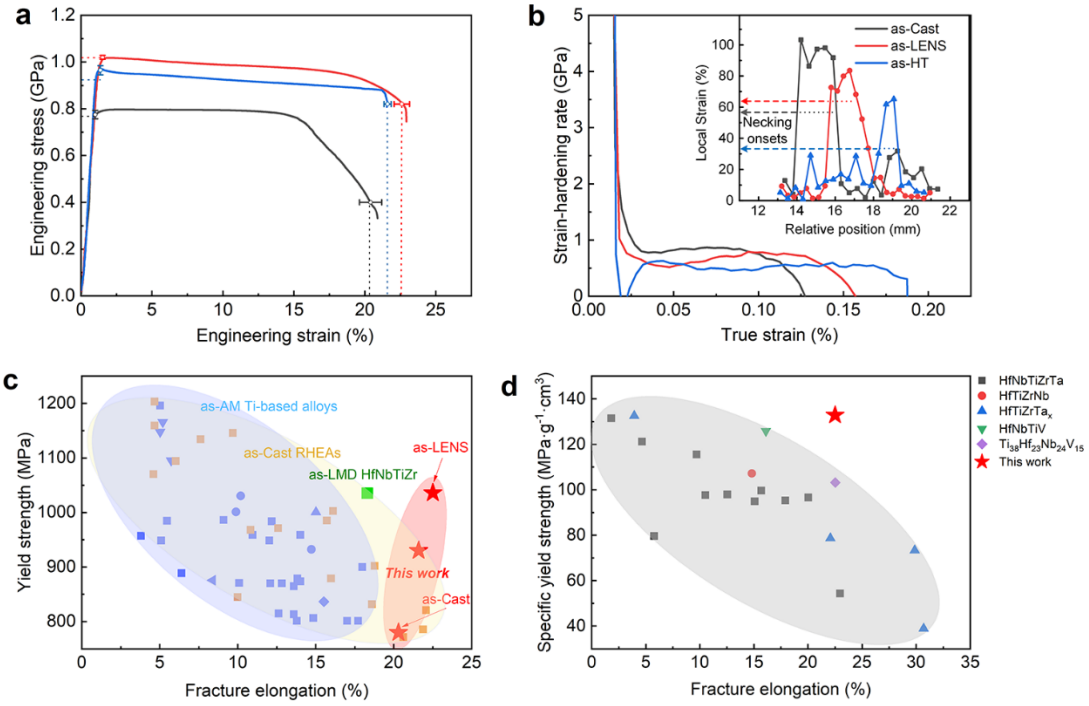

Fig. 9 The improved tensile strength-ductility synergy achieved in as-LENS RHEA compared to those fabricated via different approaches. a, The engineering stress-strain curves of RHEAs fabricated different approaches. **b,** The corresponding strain hardening rate curves show different deformation stages. Insert of **b** is the local strain profiles by DIC. **c,** the tensile yield strength versus fracture elongation in comparison with previously reported Ti-based alloys prepared via AM methods [14], the bcc-type RHEAs [4] as well as the as-LENS HfNbTiZr RHEA [21]. **d,** giving the comparison with previously reported RHEAs on the specific yield strength versus the fracture elongation.

The fracture surface morphologies show the presence of complete ductile dimples without forming cleavages or intergranular fracture surfaces (see **Fig. 10a-c**), indicating the formation of through-sample ductile fractures in those RHEAs. **Fig. 10d** depicts the splicing BSE images of upper tensile surfaces from RHEAs fabricated using different

methods, indicating the less uniform tensile strain in as-cast RHEA and obvious shear bands in the severely deformed zone. Due to the presence of the plateau-like plastic response in these alloys [44] (**Fig. 9b**), the Considère criterion [48] may not be applicable for predicting the onset of necking [44]. Therefore, we employed a digital image correlation measurement by involving the time-dependent methodology [49] to study the onset of necking in those RHEAs (see **Fig. 11**). **Fig. 11a** illustrates the local strain distributions of the deformed samples at the last frame before fracture, obtained through post-processed DIC results. By analyzing the time-dependence local strain increasing trends at different points (shown in **Fig. 11a**), an abrupt decrease in the time-dependence local strain curve indicates the initiation of necking [49], as demonstrated in **Fig. 11b**. Thus, the area of abrupt change (point 3) on the local strain maps (see **Fig. 11a)** can be considered as the necking boundary. As a result, the as-LENS and as-HT RHEAs exhibit larger uniform tensile strain compared to the as-cast counterpart (see **Fig. 9b** insert), which is also supported by the splicing BSE images of the tensile bar top surfaces (see **Fig. 10d**).

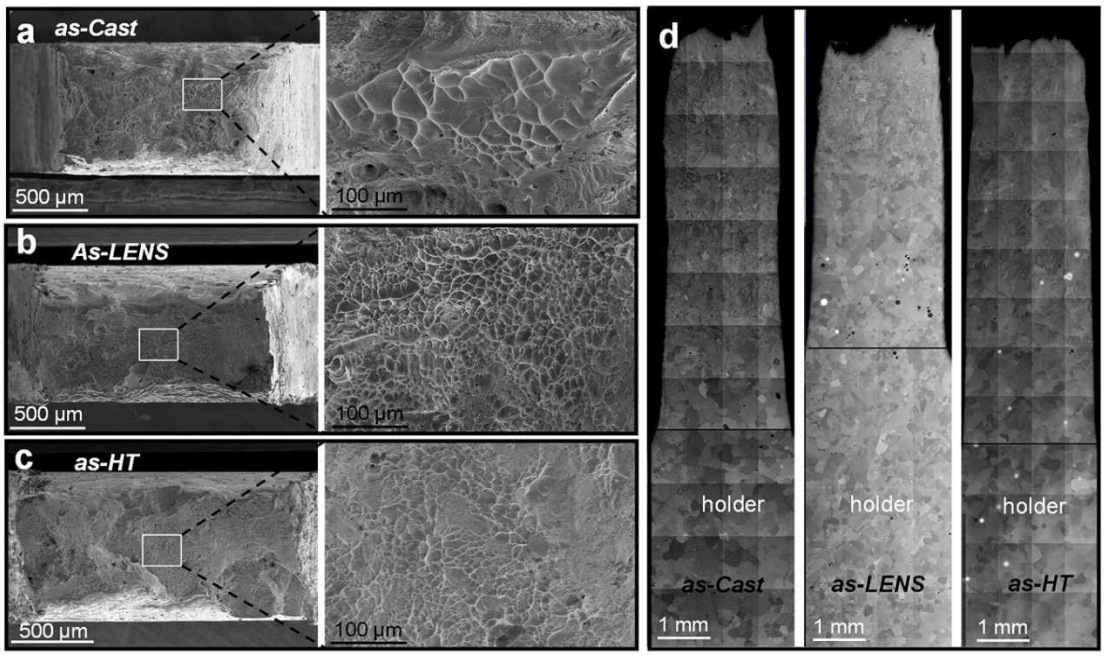

Fig. 10 Fracture morphology of $Ti_{42}Hf_{21}Nb_{21}V_{16}$ RHEAs. a-c, SEM images of fracture surfaces from as-cast, as-LENS and as-HT RHEAs, respectively, with magnified figures showing the ductile dimples without cleavages. **d,** Splicing BSE images of as-cast RHEA, as-LENS RHEA and as-HT RHEA, respectively.

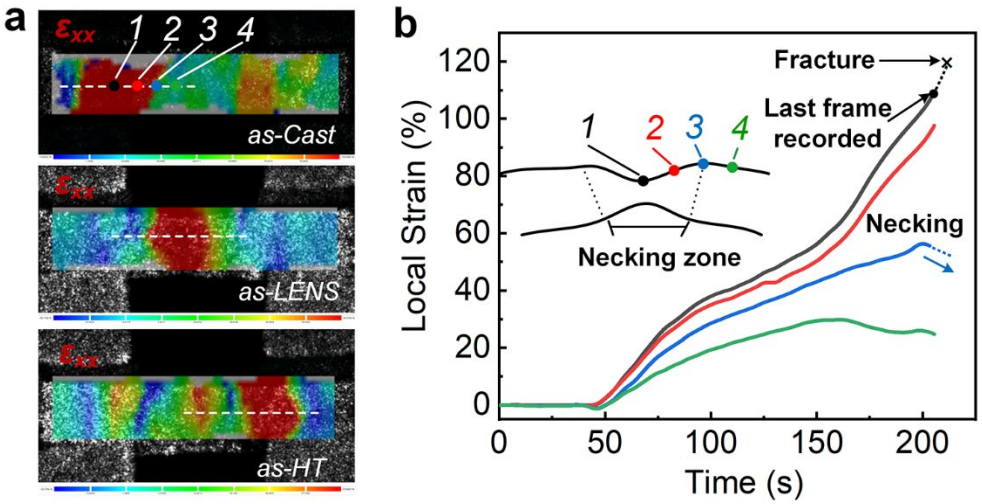

Fig. 11 Digital image correlation measurement results. a, local strain maps display the two-dimensional local strain distribution of RHEAs fabricated via different methods. **b,** The experimental time evolution of the local strain on different points (marked in **a**) shows the various increasing trends.

3.4 Deformation behavior

We then conducted the in-situ and ex-situ tensile observation on those REHAs to study their deformation behaviors. Despite having different local strains in the necking area (**Fig. 9b insert**), the RHEAs fabricated through different approaches exhibit similar deformation characteristics (**Fig. 12a**). The IPF figure near the fracture area reveals the formation of crushed grains (**Fig. 12a**). Their corresponding KAM figures in **Fig. 12b** indicate the formation of slip bands and high density of dislocations after the plastic deformation due to the higher KAM contrast in the deformed area[50], which is also revealed by the BSE images as illustrated in **Fig. 12c**. For further studying their formation mechanism, we analyzed the misorientation variations along the marked lines in **Fig. 12a**, there are slip bands formed during the deformation with the relative lower misorientations of Line 1 generally below 10°, while Line 2 exhibits larger misorientations above 15°(**Fig. 12d**) but eliminating the possibility of forming twin boundaries (generally ~50° for {332}<113> twining [21]). The formation of large-angle grain boundaries (or higher misorientations) is attributed to the presence of shear bands in highly deformed alloys, a common occurrence in highly deformed titanium [51]. At the end of the plastic deformation, the dislocation motion, excluded from the deform-induced phase transformation, because of the single BCC formed after deformation demonstrated in **Fig. 12e**, accompanied by the shear band deformation to induce the local stress concentration and crystal-crushing to form new grains.

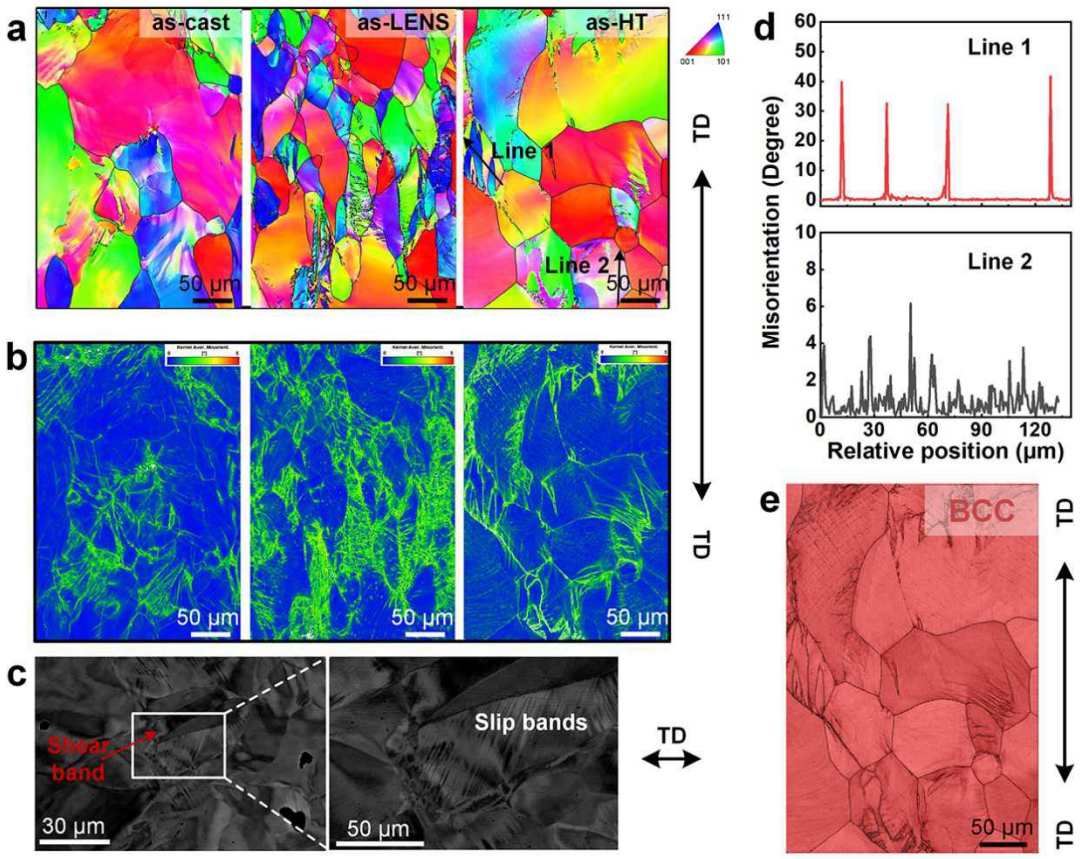

Fig. 12 Microstructure evolution of different approach fabricated $Ti_{42}Hf_{21}Nb_{21}V_{16}$ RHEAs after deformation. a, The EBSD IPF maps and **b**, KAM figures collected near the fracture areas from the corresponding RHEAs fabricated using different methods. **c**, BSE image of the deformed area. **d**, The corresponding local misorientation variation along the lines marked in **a. e**, The EBSD phase image of as-HT RHEA gives that only a single BCC was formed after deformation.

To study the dislocation evolution during the deformation, in-situ tensile testing was conducted in TEM on the LENS-fabricated specimen, which exhibits excellent strength-ductility synergy. During the in-situ tensile test, the deformation was terminated at certain pre-strains. At the early plastic deformation stage (~2%), the formation of dislocation dipoles as well as dislocation loops indicates the role of screw dislocations in the plastic deformation process. A dislocation pinning effect can occur in that deformation stage in **Fig. 13a (iii)**. As the sample was strained to 5%, continuous

planar-slip bands and high density of dislocations dominated this deformation stage (**Fig. 13b**). With further straining, the cross-slip is further promoted in this RHEA, and with the characteristics of wavy slip (**Fig. 13c (i)**) [52], dominating the plastic flow at this deformation stage. Additionally, the formation of dislocation walls is also observed (**Fig. 13c (ii)**) and the SAED pattern **Fig. 13d** indicates no phase or twin formation during deformation. The inverse Fourier transformation image from the HRTEM image of the deformed area (**Fig. 13e (i)**) confirms the presence of mixed dislocations of both the edge and screw characters, as shown in **Fig. 13e (ii)**.

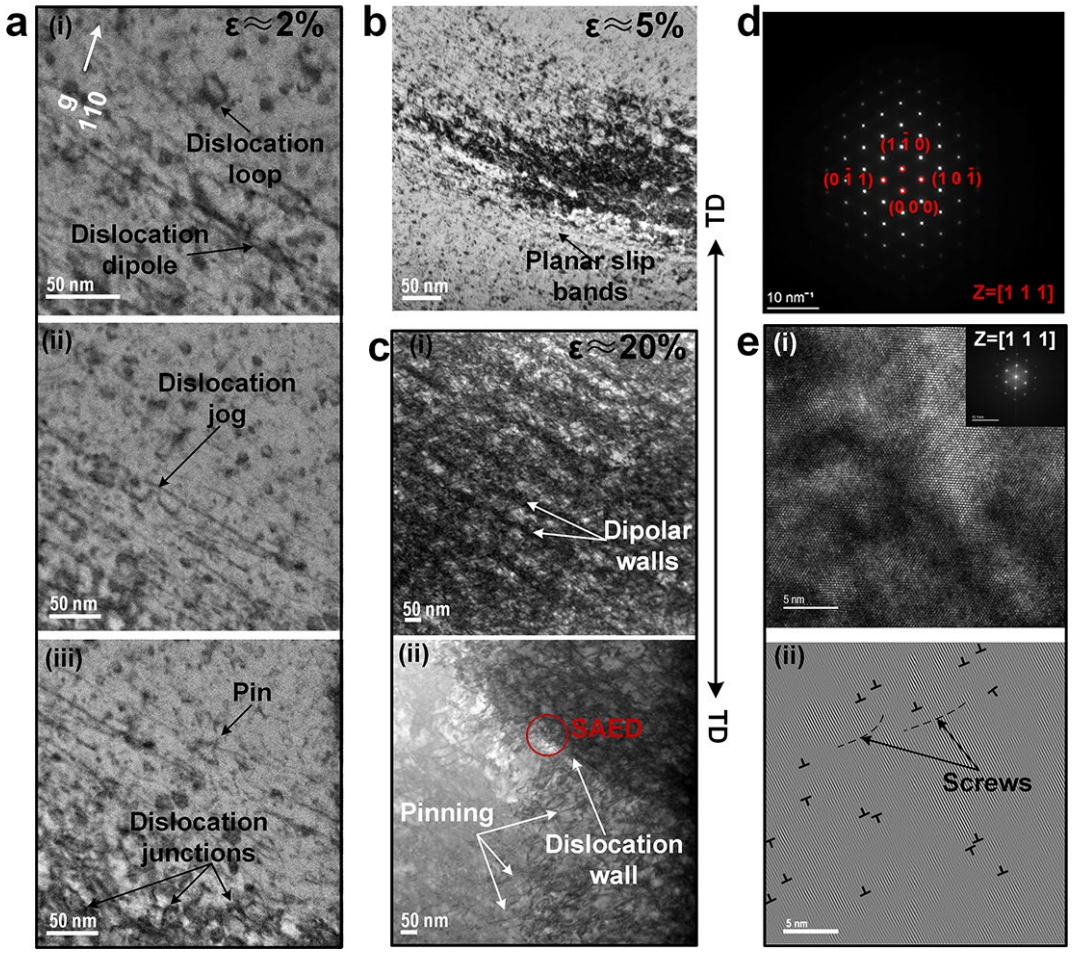

Fig. 13 In situ deformed microstructure observations. a (i-iii), The TEM bright field (BF) image of the as-LENS RHEAs at a terminated strain of 2%. **b,** TEM BF figure of the deformed microstructure at a strain of 5%. **c(i),** Deformed microstructure at a strain of 20% showing the formation of dipolar walls and **c(ii)** formed dislocation wall accompanied with dislocation pinning effects. **d,** SAED pattern of marked area in **c(i) e(i),** HRTEM image of deformed microstructure collected along [111] zone axis with corresponding FFT image insert and **d(ii),** The corresponding iFFT figure shows the presence of mixed edge and screw dislocations with huge density.

4. Discussion

4.1 The origins of ductility in selected RHEA

The stacking fault energy plays a crucial role in regulating the stacking fault in FCC-based HEAs, which in turn can generate deformed twins [53] to strengthen these

HEAs. Although BCC-based materials have equivalent slipping systems as FCC-based alloys, the lower stacking compact on the slipping surfaces in BCC-based materials compared to FCC-based alloys is responsible for the even worsened ductility in BCC-based metals. The stacking fault energy (SFE) is a useful parameter for estimating the ductility levels in BCC-based materials, with higher SFE leading to lower ductility in BCC-based materials [54]. The dislocation movement near the crack tip would affect crack growth and further reflect the fracture characteristics. Rice et al. [55] established a relationship between the critical crack propagation force for I-type crack (G_c) and the unstable stacking fault energy (γ_{us}), as shown in the following function:

$$G_c' = 8\frac{1+(1-v)tan^2\theta}{(1+cos\varphi)sin^2\varphi}\gamma_{us} \qquad \text{Eq. 3}$$

where v is Poisson's ratio, θ is the angle between the initial cracking and prolonging directions, φ represents the angle between the cracking lattice plane and slip planes.

According to the Griffith fracture theory [56], the cracking expansion force (G_c), known as the brittle cracking critical energy, is determined by surface energy (γ_s), given as follows:

$$G_c = 2\gamma_s \qquad \text{Eq. 4}$$

As a result, when G_c is higher than G_c', the dislocation nucleation occurs near the crack tips, resulting in ductile fracture; otherwise, cracking expansion would be formed, leading to brittle fracture. When $G_c > G_c'$, the following equation can be derived:

$$\frac{\gamma_s}{\gamma_{us}} = 4\frac{1+(1-v)tan^2\theta}{(1+cos\varphi)sin^2\varphi} \qquad \text{Eq. 5}$$

Hu et al. [54] used a factor of D, the ratio of γ_s and γ_{us}, which can be used for predicting the ductile level in RHEAs. When D exceeds 3.5, the fabricated RHEAs generally have a higher compressive fracture strain [54], indicating the occurrence of dislocation nucleation before cracking, resulting in ductile fracture [55]. The ratio between the surface energy (γ_s) and (γ_{us}) greatly exceeds the criteria for ductile or brittle materials, indicating that the dislocation nucleation precedes the crack formation. On the other hand, the stress field near the crack tip can also influence crack propagation. For instance, tensile stress near the crack tip promotes cracks to overcome the energy barrier for crack formation, while shear stress at the crack tip promotes ductility by facilitating dislocation or stacking fault motion to overcome the energy barrier from USFE [57]. Mei et al. [58] introduced a dimensionless factor of ξ to estimate the ductile-brittle properties, demonstrating that:

$$\xi = \frac{\gamma_s}{\gamma_{us}} cot\frac{\theta}{2} \qquad \text{Eq. 6}$$

We can realize that the ductile-brittle properties of I-type cracks are influenced by the surface energy, the USFE as well as the cracking angle. For materials with the same surface energy and USFE, the angle between the initial cracking direction and prolonging direction determines the brittle-ductile properties. When the initial cracking and prolonging directions have a smaller angle, a brittle fracture characteristic is produced, otherwise, the materials have ductile fracture properties. Hence, the designed

RHEA system in this study exhibits the characteristics of ductile materials, making it suitable for the additive manufacturing process.

4.2 Intrinsic strength of selected RHEA

By utilizing additive manufacturing processes on metallic materials, especially those alloys with FCC phase structure, the effect on the strength-ductility trade-off contributes to the unique heterogeneous structures [12] as well as the dislocation network [11]. While there are other methods such as refinement grains strengthening [59], the twining or transformation-induced plasticity [9], and even the local chemical order [60] that can potentially enhance the strength of alloys while maintaining ductility, these approaches are absent in this study. To better understand the effects on yield strength, the contributions to the yield strength are typically considered as follows [21]:

$$\sigma_y = (\sigma_{0.2})_{mix} + \sigma_G + \sigma_S + \sigma_D + \sigma_P \qquad \text{Eq. 7}$$

4.2.1 Mixed intrinsic yield strength of pure metals

In **Eq. 7**, $(\sigma_{0.2})_{mix}$ refers to the mixed intrinsic yield strength of pure metals, which can be expressed using the rule of mixtures:

$$(\sigma_{0.2})_{mix} = \sum c_i \, \sigma_{0.2i} \qquad \text{Eq. 8}$$

where c_i and $\sigma_{0.2i}$ denote the atomic fraction of i_{th} element and its yield strength at the given temperature respectively, as listed in **Table 2**. Consequently, the calculated value of $(\sigma_{0.2})_{mix}$ for $Ti_{42}Hf_{21}Nb_{21}V_{16}$ RHEA is 203.22 MPa.

Table 2 Basic physical properties of pure constituents of the fabricated RHEAs where the yield strength of pure Ti, Nb and V was obtained from Ref. [60] while that of pure Hf was collected via Ref. [61].

Element	Ti	Hf	Nb	V
Melting point (K)	1941	2506	2750	2183
R (pm)	140	155	145	135
G (GPa)	44	30	38	47
Yield strength/ MPa	225	230	114	228
Atomic fraction	0.42	0.21	0.21	0.16

4.2.2 Grain boundary strengthening value

In **Eq. 7**, σ_G is the strength attributed to the grain boundary strengthening, which is given as follows [62]:

$$\sigma_G = \sigma_f + K_{HP} \cdot d^{-0.5} \qquad \text{Eq. 9}$$

where K_{HP} and d are the Hall-Petch coefficient and grain diameter respectively, σ_f represents the lattice friction stress, which can be replaced by the Peierls-Nabarro (P-N) stress (σ_{P-N}) [63], given by:

$$\sigma_f = \sigma_{P-N} = G\exp(-2\pi d/b) \quad \text{Eq. 10}$$

where G denotes the shear modulus which can be obtained by the rule of mixtures, b is the burgers vector and d represents the temperature-dependent dislocation width, demonstrated as follows:

$$d = d_0(1 + \alpha T) \quad \text{Eq. 11}$$

in which d_0 denotes the dislocation core at absolute zero and α is a constant, approximately equal to the reciprocal of the melting temperature ($\frac{1}{T_m}$), and T is the test temperature (298 K). Using the rule of mixtures, the melting point (T_m) and shear modulus (G) are calculated to be 2668 K and 40.28 GPa, respectively. When $d_0 = b$, the friction stress (σ_f) is calculated to be 37.29 MPa. For the Hall-Petch coefficient, Sriharitha et al. [64] provided an estimation using the following equation:

$$K_{HP} \approx 0.05G\sqrt{b} \quad \text{Eq. 12}$$

where b is the burgers vector which is used to calculate K_{HP} as 35.59 MPa·μm$^{-1/2}$. Based on the EBSD grain size collection results and **Eq. 9**, the contribution to the yield stress from the grain boundaries is 39.54 MPa in the as-cast RHEA samples.

4.2.3 Solid strengthening in RHEA

Unlike conventional metallic materials, HEAs exhibit superior mechanical strength due to lattice distortion, which induces a significant solid solution strengthening effect [27]. The nature of solid solution strengthening arises from the interactions between dislocations and distorted stress fields from the solute [65]. Wang

et al. [63] gave an expression that considers the contribution of lattice distortion and modulus mismatch as follows,

$$\sigma_S = \sum_i^n (AGc_i^{\frac{2}{3}}\delta_i^{\frac{4}{3}} + BGc_i\delta_i) \qquad \text{Eq. 13}$$

where A and B are dimensionless constants of 0.1 and 0.03, respectively. [27,66]. c_i is the atomic fraction of i_{th} consistent, δ_i is the stress contribution from i_{th} consistent in terms of lattice distortion as well as the modulus mismatch. Based on Labusch's model [66], the modified models express the lattice distortion (δr_i) and the modulus mismatch (δG_i), and the calculated results, given in **Table 3**, are expressed as follows [27],

$$\delta r_i = \frac{9}{8} \cdot \sum_{i \neq j} c_j \cdot \delta r_{ij} \qquad \text{Eq. 14}$$

$$\delta G_i = \frac{9}{8} \cdot \sum_{i \neq j} c_j \cdot \delta G_{ij} \qquad \text{Eq. 15}$$

where $\delta r_{ij} = 2(r_i - r_j)/(r_i + r_j)$ and $\delta G_{ij} = 2(G_i - G_j)/(G_i + G_j)$ provide details of the atomic radius and shear modulus differences between the i_{th} and j_{th} atoms, respectively, listed in **Table 4**. The properties of the constituents are listed in **Table 2**, by which the calculated solid solution stress is 468.25 MPa.

Table 3 The calculated atomic modulus and atomic size mismatch.

Element	Ti	Hf	Nb	V
δr_i	-0.0258	0.0886	0.0137	-0.0667
δG_i	0.1120	-0.3136	-0.0517	0.1854

Table 4 Calculated values for atomic radius mismatch of δr_{ij} (underlined numbers) and shear modulus difference of δG_{ij} for different atomic pairs.

Element i/j $\underline{\delta r_{ij}}/\delta G_{ij}$	Ti	Hf	Nb	V
Ti	0	0.3780	0.1463	-0.0659
Hf	<u>0.1017</u>	0	-0.2353	-0.441
Nb	<u>0.0351</u>	<u>-0.0667</u>	0	-0.2118
V	<u>-0.0364</u>	<u>-0.1379</u>	<u>-0.0714</u>	0

4.2.4 Dislocation strengthening in RHEA

The higher dislocation density has an impact on the yield strength, which can be determined using Taylor's hardening law [67]:

$$\Delta\sigma_D = M\alpha Gb\rho^{0.5} \qquad \text{Eq. 16}$$

in which M and α denote the Taylor factor of 3.06 [68] and correction constant of 0.3 [69], G represents the shear modulus, b is the Burgers vector and ρ gives the

dislocation density. The dislocation density can be obtained through X-ray or neutron diffraction methods, expressed in the modified Williamson-Hall plot proposed by Ungar and Borbely [70] as follows:

$$\Delta K \approx \frac{0.9}{d} + \left(\frac{\pi A b^2}{2}\right)^{\frac{1}{2}} \rho^{\frac{1}{2}} \left(K\bar{C}^{\frac{1}{2}}\right) + O(K^2\bar{C}) \qquad \text{Eq. 17}$$

where ΔK is the full width at half-maximum (FWHM). The first term in **Eq. 17** shows the grain size contribution to the line broadening and d denotes the average grain/particle size. The second term in **Eq. 17** expresses the strain contribution, mainly from the dislocation density (ρ), to the line broadening. In this term, A is a constant of 10 [71,72] for a wide range of dislocation contributions which depends on the effective outer cutoff radius of dislocations, while b is the Burgers vector. $K = 2sin\theta/\lambda$ and $\bar{C}$ denotes the average contrast factor of dislocations of the *hkl* indices under different reflections [73]:

$$\bar{C} = \bar{C}_{h00}\left(1 - q\frac{h^2k^2+h^2l^2+k^2l^2}{(h^2+k^2+l^2)^2}\right) \qquad \text{Eq. 18}$$

where $\bar{C}_{h00}$ and q are the constants determined by the elastic constants, especially the elastic anisotropy $A_i = 2C_{44}/(c_{11} - c_{12})$ and the ratio of c_{11}/c_{44}. Based on the calculated elastic stiffness constants (C_{11}=161.326 GPa, C_{44}=49.034 GPa) using a VCA model by CASTEP after the convergence test, the $A_i = 2.08$ and $\frac{c_{11}}{c_{44}} = 3.29$. When edge and screw dislocations have an equal proportion, the $\bar{C}_{h00}$ can be obtained according to Ref [74] as 0.25884. The last term in **Eq. 17** refers to the higher order of $K^2\bar{C}$, which can be considered negligible. Hence, the **Eq. 17** can also be rewritten as [75]:

$$(\Delta K)^2 \approx \left(\frac{0.9}{d}\right)^2 + \frac{\pi A b^2}{2}\rho K^2 \bar{C} \qquad \text{Eq. 19}$$

By inserting **Eq. 18** into **Eq. 19** yields:

$$[(\Delta K)^2 - \alpha]/K^2 \approx \beta \bar{C}_{h00}(1 - qH^2) \qquad \text{Eq. 20}$$

where $\alpha = \left(\frac{0.9}{d}\right)^2$ and $\beta = \frac{\pi A b^2}{2}\rho$. By plotting $[(\Delta K)^2 - \alpha]/K^2$ versus H^2 [74], we can obtain a q value of 0.9355. Depending on **Eq. 17**, The FWHM of $Ti_{42}Hf_{21}Nb_{21}V_{16}$ RHEA versus the $K\bar{C}^{\frac{1}{2}}$, gives a slope value of $\left(\frac{\pi A b^2}{2}\right)^{\frac{1}{2}}\rho^{\frac{1}{2}}$. As a result, the dislocation density in the as-cast $Ti_{42}Hf_{21}Nb_{21}V_{16}$ RHEA is around 1.16 $\times 10^{13}$ m^{-2}. By **Eq. 16**, we can obtain the dislocation contribution to the yield strength as 37.16 MPa. The dislocation densities of as-LENS as well as the as-HT are 6.15 $\times 10^{13}$ m^{-2} and 1.40$\times$ 10^{13} m^{-2}, respectively. Therefore, the contribution to the yield strength in the as-LENS as well as the as-HT samples are 85.56 MPa and 40.77 MPa, respectively.

4.3 Mechanisms of improved strength-ductility synergy

The as-LENS $Ti_{42}Hf_{21}Nb_{21}V_{16}$ RHEA exhibits the best strength-ductility synergy among those fabricated via other methods. In general, the mixed yield strength from the pure metals, the intrinsic solid-solution strengthening, the grain boundary strengthening as well as the dislocation strengthening [21] contribute to the yield strength of the RHEA. Since those RHEAs have the same nominal compositions, the mixed yield strength and the intrinsic solid strength, considering the atomic radius and shear modulus mismatch [27], are expected to be the same. Although there are grain size differences among the fabricated REHAs, the Hall-Petch coefficient shows that the shear modulus sensitivity has a relatively low level, resulting in an insignificant effect

of grain size difference on the yield strength. The KAM figures (**Fig. 6c**) do not show significant dislocation differences, but the modified Williamson-Hall method [70] reveals subtle differences in dislocation densities among the RHEAs fabricated using different approaches.

Specifically, the as-LENS RHEA exhibits the highest dislocation density (~6.5× 10^{13} m^2), which is 2 orders of magnitude lower than that in FCC alloys fabricated via AM methods [76] to form the dislocation networks. Although the contribution of dislocation strengthening to the yield strength in the LMD-fabricated HfNbTiZr RHEA was neglected [21], the dislocation density fluctuations were observed in RHEAs fabricated via different approaches. Comparing the as-cast and annealed samples, the LENS-fabricated RHEAs show an increase of ~ 40 MPa increase in yield strength compared to the as-HT sample, as calculated using Taylor's hardening law [67], which can account for the decreased value of a yield strength after annealing (**Fig. 9a**). However, there is still a question regarding the increase in yield strength from the as-cast sample to the as-LENS sample, as the nominal composition, grain size and dislocation densities are similar (as listed in **Table 5**).

Table 5 The calculated values of contributions to the yield strength and the experimental results of $Ti_{42}Hf_{21}Nb_{21}V_{16}$ RHEAs with the errors between the calculated and experimental results are at an acceptable level.

$(\sigma_{0.2})_{mix}$	σ_S	σ_G	σ_D	σ_{s-i}	σ_{y-cal}	σ_{y-exp}

As-cast			39.54	37.16	-	748.17	780
As-LENS	203.22	468.25	39.84	85.56	178.36	975.23	1030
As-HT			39.54	40.77	177.46	929.24	970

Although the nano-scale heterogeneity, like the local chemical fluctuations [21], the local chemical order (LCO) [60], even the nano-scale secondary phase (BCT) [44], as well as the nano ceramic particles [77] etc., has been proven to be effective in improving the mechanical performance of HEAs, these structures generally a great influence on ductility through their interaction with dislocations than strength. In our study, we conducted nitrogen and oxygen (N&O) tests on the RHEAs fabricated using different approaches, considering that the BCC matrix in the as-LENS RHEA has a higher lattice constant than the as-cast counterpart (**Fig. 7b**). The results showed an increase in oxygen and nitrogen content in the LENS-fabricated RHEA compared to those in as-cast one, ~0.02 at.% (oxygen) and ~0.10 at.% (nitrogen) (**Table 1**), respectively. Based on the oxygen/nitrogen analysis results, the LENS-fabricated sample has higher O/N contents compared to the as-cast one, while those contents are similar in the as-LENS and as-HT samples. Interstitial atom strengthening, such as oxygen and nitrogen, has been proven to significantly improve the yield strength of the HfNbTiZr RHEA by forming the ordered complexes [9]. In general, square distortion is generally attributed to the solid solution by interstitial atoms, resulting in the

appearance of significant shear strain. During the room temperature deformation, the screw dislocations play a crucial role in work hardening [78], interacting with the square distortion center [68]. Fleishcher [79] provided an estimation of yield strength increase resulting from the square distortion in the following equation,

$$\Delta\sigma = \frac{G\Delta\varepsilon c^{1/2}}{3} \qquad \text{Eq. 21}$$

where $\Delta\varepsilon$ is the difference between the longitudinal and transverse strain in the square distortion. Based on the experimental results in the oxygen-doped $Ti_{41}V_{27}Hf_{15}Nb_{15}$ RHEA [80], the difference between the longitudinal and transverse strains resulting from an oxygen solid solution ($\Delta\varepsilon_O$) is estimated to be 0.338, while $\Delta\varepsilon_N$ is calculated to be 0.275 based on the N-doped HfNbTiZr study [9]. Consequently, the yield strength increase from the interstitial atom strengthening is estimated to be ~ 178 MPa, which accounts for the increase of yield strength in the LENS-fabricated RHEA compared to the as-cast RHEA. In conclusion, the increase of yield strength in the LENS-fabricated RHEA compared to the as-cast sample is mainly attributed to the solid-soluble interstitial atoms in the RHEA matrix, while the slightly decreased dislocation density would account for the yield strength decrease in the as-HT samples compared to the LENS-fabricated RHEA. These results demonstrate that limited interstitial atoms in RHEAs would not embrittle the fabricated sample but instead increase the yield strength, which can also explain the yield strength increase when comparing the yield strength between the LMD-fabricated HfNbTiZr (1030 MPa) [21] and as-cast HfNbTiZr alloy (750 MPa) [9].

We then proceeded to discuss the improved ductility observed in LENS-fabricated $Ti_{42}Hf_{21}Nb_{21}V_{16}$ RHEA. During the early plastic deformation stage (~2%), considerable dislocation loops and dipoles were initially formed (**Fig. 13a**), indicating the occurrence of multiple dislocation interactions [52]. Under continuous external stress, dislocation junctions and dislocation jogs were formed and induced by triggering multiple slip systems [81], facilitated by the presence of interstitial atoms [78], which can hinder the motion of lateral and cross kinks[78]. As depicted in **Fig. 13a**, a dislocation pinning effect can be observed during this deformation stage.

By straining the sample to 5%, continuous coplanar-slipped dislocations (**Fig. 13b**) are mainly triggered by external stress, resulting from the glide plane softening phenomenon and the reduced energy barrier on the same gliding plane for the successive dislocations [82]. The LENS-fabricated sample exhibits phase segregation (**Fig. 8b(iii)**) due to the complex thermal history during the additive procedure [19]. During the deformation, the phase interfaces would make the dislocation motion sluggish and even retard the movement of dislocations [6]. The large interfacial lattice distortion (**Fig. 8d(iii)**) acts as an effective barrier for dislocation motion. After loading, the stored dislocations necessitate cross-slip to promote the stuck screw dislocations, which is the key factor in controlling the ductility as well as the strain hardening [78], to move forward to the barrier [6]. The inverse Fourier transformation image confirms the presence of mixed dislocations of both the edge and screw characters, as shown in **Fig. 13d(ii)**.

With further straining, the cross-slip is further promoted in the LENS-fabricated RHEA, dominating the plastic flow at this deformation stage with wavy slip characteristics [52]. Apart from the cross-slip of the dislocations, similar to other bcc-type RHEAs like the TiZrHfNbTa RHEA, the formation of dislocation loops as well as dipoles is attributed to the work hardening rate [83], and cross-slip of screw dislocations prevails during deformation to form the dipolar walls [9,84]. The high density of the dislocation walls (DWs) is also formed on account of the successive cross-slip, as shown in **Fig. 13c(ii).** The complex interactions between the cross-slip and DWs promote dislocation reactions, multiplication and storage [6], resulting in an increasing strain hardening rate during this deformation stage. Additionally, the presence of interfaces would retard the movement of dislocations [6] and generate the reverse interface energy [44], leading to increased dislocation slip resistance to strain hardening and delaying the formation of necking. Furthermore, the local chemical fluctuations (**Fig. 8d**) can alter the local SFE to modify the motion path of the screw dislocation cores, by increasing the energy barrier for dislocation motion, and thereby improving the intrinsic ductility [85].

5. Conclusions

In summary, we propose an AM process involving the remelting and low oxygen & nitrogen environment to fabricate $Ti_{42}Hf_{21}Nb_{21}V_{16}$ RHEAs with significantly enhanced mechanical properties. The main conclusions of this study are as follows,

1) A $Ti_{42}Hf_{21}Nb_{21}V_{16}$ RHEA was selected RHEA for LENS fabrication due to its ductile nature, which was verified via DFT calculation. The LENS-fabricated $Ti_{42}Hf_{21}Nb_{21}V_{16}$ RHEA exhibits a giga-pascal yield strength with a fracture strain higher than 22 %, a level that is difficult to achieve through casting.

2) The LENS procedure induces a complex thermal-stress environment and ultra-fast cooling rate, which promotes the decomposition of the BCC matrix and the formation of a coherent interface. These interfaces act as barriers to dislocation motion, thereby enhancing the ductility. By applying heat treatment on the LENS-fabricated sample, the BCC matrix decomposition is further promoted, leading to improved uniform deformation without significantly sacrificing the yield strength.

3) RHEAs with similar nominal compositions, fabricated through different approaches, exhibit approximate intrinsic yield strength. The increase in yield strength from the as-cast one to the as-LENS RHEA is attributed to the interstitial atom strengthening, rather than the formation of commonly found dislocation networks in FCC-based alloys fabricated through the AM process.

4) This study provides novel insights into overcoming the strength-ductility trade-off of RHEA, not only by tailoring the microstructures but also more importantly by regulating the composition during the manufacturing process.

Acknowledgements

This work was financially supported by the joint research scheme of National Natural Science Foundation of China (NSFC) and Research Grants Council of Hong Kong (RGC) (No. 52061160483 and No. N_PolyU523/20), Guangdong Major Project of Basic and Applied Basic Research, China (Grant No. 2019B030302010), the National Key Research and Development Program of China (Grant No. 2021YFA0716302), Guangdong Basic and Applied Basic Research, China (Grant No. 2020B1515130007), and the National Natural Science Foundation of China (Grant Nos. 52104362 and 52001221).

Declaration of Competing interests

There authors have no competing interests to declare.

CRediT authorship contribution statement

Y. Zhang: Conceptualization, Methodology, Software, Formal analysis, Data Curation, Writing- Original Dragt, Writing- Review & Editing. **B. Qin**, **C. Feng**, **S. Ye, Y. Yan**: Methodology, Investigation. **D. Ouyang, L. Liu**: revision, review & editing. **H. Ke**: Conceptualization, Supervision, Writing – review & editing. **K. C. Chan**: Conceptualization, Supervision, Project acquisition, Funding acquisition, Writing – review & editing. **W. Wang**: Conceptualization, Supervision, Funding acquisition. Writing – review & editing.

References

[1] J. Yeh, S. Chen, S. Lin, J. Gan, T. Chin, T. Shun, C. Tsau, Nanostructured High-Entropy Alloys with Multiple Principal Elements : Novel Alloy Design Concepts and Outcomes, Adv. Eng. Mater. 6 (2004) 299–303. https://doi.org/10.1002/adem.200300567.

[2] B. Cantor, I.T.H. Chang, P. Knight, A.J.B. Vincent, Microstructural development in equiatomic multicomponent alloys, Mater. Sci. Eng. A. 375–377 (2004) 213–218. https://doi.org/10.1016/j.msea.2003.10.257.

[3] O.N. Senkov, G.B. Wilks, D.B. Miracle, C.P. Chuang, P.K. Liaw, Refractory high-entropy alloys, Intermetallics. 18 (2010) 1758–1765.

[4] O.N. Senkov, D.B. Miracle, K.J. Chaput, J.P. Couzinie, Development and exploration of refractory high entropy alloys - A review, J. Mater. Res. 33 (2018) 3092–3128. https://doi.org/10.1557/jmr.2018.153.

[5] D.B. Miracle, O.N. Senkov, A critical review of high entropy alloys and related concepts, Acta Mater. 122 (2017) 448–511. https://doi.org/10.1016/j.actamat.2016.08.081.

[6] Z. An, S. Mao, T. Yang, C.T. Liu, B. Zhang, E. Ma, H. Zhou, Z. Zhang, L. Wang, X. Han, Spinodal-modulated solid solution delivers a strong and ductile refractory high-entropy alloy, Mater. Horizons. 8 (2021) 948–955. https://doi.org/10.1039/d0mh01341b.

[7] Z. Li, K.G. Pradeep, Y. Deng, D. Raabe, C.C. Tasan, Metastable high-entropy dual-phase alloys overcome the strength-ductility trade-off, Nature. 534 (2016) 227–230. https://doi.org/10.1038/nature17981.

[8] Y. Bu, Y. Wu, Z. Lei, X. Yuan, H. Wu, X. Feng, J. Liu, J. Ding, Y. Lu, H. Wang, others, Local chemical fluctuation mediated ductility in body-centered-cubic high-entropy alloys, Mater. Today. 46 (2021) 28–34.

[9] Z. Lei, X. Liu, Y. Wu, H. Wang, S. Jiang, S. Wang, X. Hui, Y. Wu, B. Gault, P. Kontis, D. Raabe, L. Gu, Q. Zhang, H. Chen, H. Wang, J. Liu, K. An, Q. Zeng, T.G. Nieh, Z. Lu, Enhanced strength and ductility in a high-entropy alloy via ordered oxygen complexes, Nature. 563 (2018) 546–550. https://doi.org/10.1038/s41586-018-0685-y.

[10] H. Huang, Y. Wu, J. He, H. Wang, X. Liu, K. An, W. Wu, Z. Lu, Phase-Transformation Ductilization of Brittle High-Entropy Alloys via Metastability Engineering, Adv. Mater. 29 (2017). https://doi.org/10.1002/adma.201701678.

[11] L. Liu, Q. Ding, Y. Zhong, J. Zou, J. Wu, Y.L. Chiu, J. Li, Z. Zhang, Q. Yu, Z. Shen, Dislocation network in additive manufactured steel breaks strength–ductility trade-off, Mater. Today. 21 (2018) 354–361. https://doi.org/10.1016/j.mattod.2017.11.004.

[12] Y.M. Wang, T. Voisin, J.T. McKeown, J. Ye, N.P. Calta, Z. Li, Z. Zeng, Y. Zhang, W. Chen, T.T. Roehling, R.T. Ott, M.K. Santala, P.J. Depond, M.J. Matthews, A. V. Hamza, T. Zhu, Additively manufactured hierarchical stainless steels with high strength and ductility, Nat. Mater. 17 (2018) 63–70. https://doi.org/10.1038/NMAT5021.

[13] L.C. Zhang, H. Attar, Selective Laser Melting of Titanium Alloys and Titanium Matrix Composites for Biomedical Applications: A Review, Adv. Eng. Mater. 18 (2016) 463–475. https://doi.org/10.1002/adem.201500419.

[14] Z. Liu, B. He, T. Lyu, Y. Zou, A Review on Additive Manufacturing of Titanium Alloys for Aerospace Applications: Directed Energy Deposition and Beyond Ti-6Al-4V, Jom. 73 (2021) 1804–1818. https://doi.org/10.1007/s11837-021-04670-6.

[15] C. Han, Q. Fang, Y. Shi, S.B. Tor, C.K. Chua, K. Zhou, Recent Advances on High-Entropy Alloys for 3D Printing, Adv. Mater. 32 (2020) 1–41. https://doi.org/10.1002/adma.201903855.

[16] B. Berman, 3-D printing: The new industrial revolution, Bus. Horiz. 55 (2012) 155–162. https://doi.org/10.1016/j.bushor.2011.11.003.

[17] Y. Zhang, S. Ye, H. Ke, K.C. Chan, W. Wang, In situ synthesis of N-containing CoCrFeNi high entropy alloys with enhanced properties fabricated by selective laser melting, Mater. Des. 229 (2023) 111891. https://doi.org/10.1016/j.matdes.2023.111891.

[18] Q. Li, H. Zhang, D. Li, Z. Chen, F. Wang, M. Wu, Comparative study of the microstructures and mechanical properties of laser metal deposited and vacuum arc melted refractory NbMoTa medium-entropy alloy, Int. J. Refract. Met. Hard Mater. 88 (2020) 105195. https://doi.org/10.1016/j.ijrmhm.2020.105195.

[19] T. Yang, S. Mazumder, Y. Jin, B. Squires, M. Sofield, M. V. Pantawane, N.B. Dahotre, A. Neogi, A review of diagnostics methodologies for metal additive manufacturing processes and products, Materials (Basel). 14 (2021) 1–50. https://doi.org/10.3390/ma14174929.

[20] H. Dobbelstein, E.L. Gurevich, E.P. George, A. Ostendorf, G. Laplanche, Laser metal deposition of compositionally graded TiZrNbTa refractory high-entropy alloys using elemental powder blends, Addit. Manuf. 25 (2019) 252–262. https://doi.org/10.1016/j.addma.2018.10.042.

[21] S. Gou, M. Gao, Y. Shi, S. Li, Y. Fang, X. Chen, H. Chen, W. Yin, J. Liu, Z. Lei, H. Wang, Additive manufacturing of ductile refractory high-entropy alloys via phase engineering, Acta Mater. 248 (2023) 118781. https://doi.org/10.1016/j.actamat.2023.118781.

[22] M.A. Melia, S.R. Whetten, R. Puckett, M. Jones, M.J. Heiden, N. Argibay, A.B. Kustas, High-throughput additive manufacturing and characterization of refractory

high entropy alloys, Appl. Mater. Today. 19 (2020) 100560. https://doi.org/10.1016/j.apmt.2020.100560.

[23] M. Moorehead, K. Bertsch, M. Niezgoda, C. Parkin, M. Elbakhshwan, K. Sridharan, C. Zhang, D. Thoma, A. Couet, High-throughput synthesis of Mo-Nb-Ta-W high-entropy alloys via additive manufacturing, Mater. Des. 187 (2020) 108358. https://doi.org/10.1016/j.matdes.2019.108358.

[24] H. Dobbelstein, M. Thiele, E.L. Gurevich, E.P. George, A. Ostendorf, Direct metal deposition of refractory high entropy alloy MoNbTaW, Phys. Procedia. 83 (2016) 624–633. https://doi.org/10.1016/j.phpro.2016.08.065.

[25] P. Gu, T. Qi, L. Chen, T. Ge, X. Ren, Manufacturing and analysis of VNbMoTaW refractory high-entropy alloy fabricated by selective laser melting, Int. J. Refract. Met. Hard Mater. 105 (2022) 105834. https://doi.org/10.1016/j.ijrmhm.2022.105834.

[26] H. Dobbelstein, E.P. George, E.L. Gurevich, A. Kostka, A. Ostendorf, G. Laplanche, Laser metal deposition of refractory high-entropy alloys for high-throughput synthesis and structure-property characterization, Int. J. Extrem. Manuf. 3 (2020). https://doi.org/10.1088/2631-7990/abcca8.

[27] O.N. Senkov, J.M. Scott, S. V. Senkova, D.B. Miracle, C.F. Woodward, Microstructure and room temperature properties of a high-entropy TaNbHfZrTi alloy, J. Alloys Compd. 509 (2011) 6043–6048. https://doi.org/10.1016/j.jallcom.2011.02.171.

[28] I. Kunce, M. Polanski, J. Bystrzycki, Structure and hydrogen storage properties of a high entropy ZrTiVCrFeNi alloy synthesized using Laser Engineered Net Shaping (LENS), Int. J. Hydrogen Energy. 38 (2013) 12180–12189. https://doi.org/10.1016/j.ijhydene.2013.05.071.

[29] M. Polanski, M. Kwiatkowska, I. Kunce, J. Bystrzycki, Combinatorial synthesis of alloy libraries with a progressive composition gradient using laser engineered net shaping (LENS): Hydrogen storage alloys, Int. J. Hydrogen Energy. 38 (2013) 12159–12171. https://doi.org/10.1016/j.ijhydene.2013.05.024.

[30] I. Kunce, M. Polanski, J. Bystrzycki, Microstructure and hydrogen storage properties of a TiZrNbMoV high entropy alloy synthesized using Laser Engineered Net Shaping (LENS), Int. J. Hydrogen Energy. 39 (2014) 9904–9910. https://doi.org/10.1016/j.ijhydene.2014.02.067.

[31] R. Montanari, G. Costanza, M.E. Tata, C. Testani, Lattice expansion of Ti-6Al-4V by nitrogen and oxygen absorption, Mater. Charact. 59 (2008) 334–337. https://doi.org/10.1016/j.matchar.2006.12.014.

[32] S.J. Clark, M.D. Segall, C.J. Pickard, P.J. Hasnip, M.I.J. Probert, K. Refson, M.C. Payne, First principles methods using CASTEP, Zeitschrift Fur Krist. 220 (2005) 567–570. https://doi.org/10.1524/zkri.220.5.567.65075.

[33] B. Zheng, Y. Zhou, J.E. Smugeresky, J.M. Schoenung, E.J. Lavernia, Thermal behavior and microstructural evolution during laser deposition with laser-engineered net shaping: Part I. Numerical calculations, Metall. Mater. Trans. A Phys. Metall. Mater. Sci. 39 (2008) 2228–2236. https://doi.org/10.1007/s11661-008-9557-7.

[34] K. Choudhary, F. Tavazza, Convergence and machine learning predictions of Monkhorst-Pack k-points and plane-wave cut-off in high-throughput DFT calculations, Comput. Mater. Sci. 161 (2019) 300–308. https://doi.org/10.1016/j.commatsci.2019.02.006.

[35] R. Mayahi, An investigation concerning generalized stacking fault behavior of AlCoxCrFeNi ($0.25 \leq x \leq 2$) high entropy alloys: Insights from first-principles study, J. Alloys Compd. 818 (2020) 152928. https://doi.org/10.1016/j.jallcom.2019.152928.

[36] J.H. Rose, J.R. Smith, J. Ferrante, Universal features of bonding in metals, Phys. Rev. B. 28 (1983) 1835–1845. https://doi.org/10.1103/PhysRevB.28.1835.

[37] X. Tian, Y. Zhu, C.V.S. Lim, J. Williams, R. Boyer, X. Wu, K. Zhang, A. Huang, Isotropic and improved tensile properties of Ti-6Al-4V achieved by in-situ rolling in direct energy deposition, Addit. Manuf. 46 (2021) 102151. https://doi.org/10.1016/j.addma.2021.102151.

[38] H. Chen, K. Kosiba, C. Suryanarayana, T. Lu, Y. Liu, Y. Wang, K.G. Prashanth, Feedstock preparation, microstructures and mechanical properties for laser-based additive manufacturing of steel matrix composites, Int. Mater. Rev. 68 (2023) 1192–1244. https://doi.org/10.1080/09506608.2023.2258664.

[39] Y. Zhong, F. Yin, T. Sakaguchi, K. Nagai, K. Yang, Dislocation structure evolution and characterization in the compression deformed Mn-Cu alloy, Acta Mater. 55 (2007) 2747–2756. https://doi.org/10.1016/j.actamat.2006.12.012.

[40] I. Serrano-Munoz, R. Fernández, R. Saliwan-Neumann, G. González-Doncel, G. Bruno, Dislocation structures after creep in an Al-3.85 %Mg alloy studied using EBSD-KAM technique, Mater. Lett. 337 (2023) 3–6. https://doi.org/10.1016/j.matlet.2023.133978.

[41] T. Lu, N. Yao, H. Chen, B. Sun, X.Y. Chen, S. Scudino, K. Kosiba, X. Zhang, Exceptional strength-ductility combination of additively manufactured high-entropy alloy matrix composites reinforced with TiC nanoparticles at room and cryogenic temperatures, Addit. Manuf. 56 (2022) 102918. https://doi.org/10.1016/j.addma.2022.102918.

[42] C. Liu, W. Lu, W. Xia, C. Du, Z. Rao, J.P. Best, S. Brinckmann, J. Lu, B. Gault, G. Dehm, G. Wu, Z. Li, D. Raabe, Massive interstitial solid solution alloys achieve near-theoretical strength, Nat. Commun. 13 (2022) 1–9. https://doi.org/10.1038/s41467-022-28706-w.

[43] M. Klinger, A. Jäger, Crystallographic Tool Box (CrysTBox): Automated tools for transmission electron microscopists and crystallographers, J. Appl. Crystallogr. 48 (2015) 2012–2018. https://doi.org/10.1107/S1600576715017252.

[44] S. Wei, S.J. Kim, J. Kang, Y. Zhang, Y. Zhang, T. Furuhara, E.S. Park, C.C. Tasan, Natural-mixing guided design of refractory high-entropy alloys with as-cast tensile ductility, Nat. Mater. 19 (2020) 1175–1181. https://doi.org/10.1038/s41563-020-0750-4.

[45] M.J. Hÿtch, E. Snoeck, R. Kilaas, Quantitative measurement of displacement and strain fields from HREM micrographs, Ultramicroscopy. 74 (1998) 131–146. https://doi.org/10.1016/S0304-3991(98)00035-7.

[46] Y. Tong, S. Zhao, H. Bei, T. Egami, Y. Zhang, F. Zhang, Severe local lattice distortion in Zr- and/or Hf-containing refractory multi-principal element alloys, Acta Mater. 183 (2020) 172–181. https://doi.org/10.1016/j.actamat.2019.11.026.

[47] C. Lee, Y. Chou, G. Kim, M.C. Gao, K. An, J. Brechtl, C. Zhang, W. Chen, J.D. Poplawsky, G. Song, Y. Ren, Y.C. Chou, P.K. Liaw, Lattice-Distortion-Enhanced Yield Strength in a Refractory High-Entropy Alloy, Adv. Mater. 32 (2020) 1–9. https://doi.org/10.1002/adma.202004029.

[48] Y. Wang, J. Li, A. V Hamza, T.W. Barbee, Ductile crystalline-amorphous nanolaminates., Proc. Natl. Acad. Sci. U. S. A. 104 (2007) 11155–11160.

[49] A.J. Martínez-Donaire, F.J. García-Lomas, C. Vallellano, New approaches to detect the onset of localised necking in sheets under through-thickness strain gradients, Mater. Des. 57 (2014) 135–145. https://doi.org/10.1016/j.matdes.2014.01.012.

[50] S. Sandlöbes, S. Zaefferer, I. Schestakow, S. Yi, R. Gonzalez-Martinez, On the role of non-basal deformation mechanisms for the ductility of Mg and Mg-Y alloys, Acta Mater. 59 (2011) 429–439. https://doi.org/10.1016/j.actamat.2010.08.031.

[51] D. Yang, Y. An, P. Cizek, P. Hodgson, Development of adiabatic shear band in cold-rolled titanium, Mater. Sci. Eng. A. 528 (2011) 3990–3997. https://doi.org/10.1016/j.msea.2011.01.108.

[52] J. Pang, H. Zhang, L. Zhang, Z. Zhu, H. Fu, H. Li, A. Wang, Z. Li, H. Zhang, Simultaneous enhancement of strength and ductility of body-centered cubic TiZrNb multi-principal element alloys via boron-doping, J. Mater. Sci. Technol. 78 (2021) 74–80. https://doi.org/10.1016/j.jmst.2020.10.043.

[53] T.H. Lee, E. Shin, C.S. Oh, H.Y. Ha, S.J. Kim, Correlation between stacking fault energy and deformation microstructure in high-interstitial-alloyed austenitic steels, Acta Mater. 58 (2010) 3173–3186. https://doi.org/10.1016/j.actamat.2010.01.056.

[54] Y.J. Hu, A. Sundar, S. Ogata, L. Qi, Screening of generalized stacking fault energies, surface energies and intrinsic ductile potency of refractory multicomponent alloys, Acta Mater. 210 (2021) 116800. https://doi.org/10.1016/j.actamat.2021.116800.

[55] J.R. Rice, G.E. Beltz, The activation energy for dislocation nucleation at a crack, J. Mech. Phys. Solids. 42 (1994) 333–360. https://doi.org/10.1016/0022-5096(94)90013-2.

[56] A.A. Griffith, Theory of rupture, in: Proc. 1st. Int. Cong. Appl. Mech., Delft, 1924: pp. 55–63.

[57] S.G. Wang, E.K. Tian, C.W. Lung, Surface energy of arbitrary crystal plane of bcc and fcc metals, J. Phys. Chem. Solids. 61 (2000) 1295–1300. https://doi.org/10.1016/S0022-3697(99)00415-1.

[58] J. Mei, Y. Ni, J. Li, The effect of crack orientation on fracture behavior of tantalum by multiscale simulation, Int. J. Solids Struct. 48 (2011) 3054–3062. https://doi.org/10.1016/j.ijsolstr.2011.06.022.

[59] L. Lu, Y. Shen, X. Chen, L. Qian, K. Lu, Ultrahigh Strength and High Electrical Conductivity in Copper, Science (80-.). 304 (2004) 422–426. https://doi.org/10.1126/science.1092905.

[60] L. Wang, J. Ding, S. Chen, K. Jin, Q. Zhang, J. Cui, B. Wang, B. Chen, T. Li, Y. Ren, S. Zheng, K. Ming, W. Lu, J. Hou, G. Sha, J. Liang, L. Wang, Y. Xue, E. Ma, Tailoring planar slip to achieve pure metal-like ductility in body-centred-cubic multi-principal element alloys, Nat. Mater. 22 (2023). https://doi.org/10.1038/s41563-023-01517-0.

[61] A.A. Mohammed, S.M. Haris, W. Al Azzawi, Estimation of the ultimate tensile strength and yield strength for the pure metals and alloys by using the acoustic wave properties, Sci. Rep. 10 (2020) 1–12. https://doi.org/10.1038/s41598-020-69387-z.

[62] N. Hansen, Hall-petch relation and boundary strengthening, Scr. Mater. 51 (2004) 801–806. https://doi.org/10.1016/j.scriptamat.2004.06.002.

[63] Z. Wang, Q. Fang, J. Li, B. Liu, Y. Liu, Effect of lattice distortion on solid solution strengthening of BCC high-entropy alloys, J. Mater. Sci. Technol. 34 (2018) 349–354. https://doi.org/10.1016/j.jmst.2017.07.013.

[64] R. Sriharitha, B.S. Murty, R.S. Kottada, Alloying, thermal stability and strengthening in spark plasma sintered AlxCoCrCuFeNi high entropy alloys, J. Alloys Compd. 583 (2014) 419–426. https://doi.org/10.1016/j.jallcom.2013.08.176.

[65] M. Walbrühl, D. Linder, J. Ågren, A. Borgenstam, Modelling of solid solution strengthening in multicomponent alloys, Mater. Sci. Eng. A. 700 (2017) 301–311. https://doi.org/10.1016/j.msea.2017.06.001.

[66] R. Labusch, A Statistical Theory of Solid Solution Hardening, Phys. Status Solidi. 41 (1970) 659–669. https://doi.org/10.1002/pssb.19700410221.

[67] G.I. Taylor, Plastic strain in metals, J. Inst. Met. 62 (1938) 307–324.

[68] M.A. Meyers, K.K. Chawla, Mechanical behavior of materials, Cambridge university press, 2008.

[69] D.G. Kalali, S. Antharam, M. Hasan, P.S. Karthik, P.S. Phani, K. Bhanu Sankara Rao, K. V. Rajulapati, On the origins of ultra-high hardness and strain gradient plasticity in multi-phase nanocrystalline MoNbTaTiW based refractory high-entropy alloy, Mater. Sci. Eng. A. 812 (2021) 141098. https://doi.org/10.1016/j.msea.2021.141098.

[70] T. Ungár, A. Borbély, The effect of dislocation contrast on x-ray line broadening: A new approach to line profile analysis, Appl. Phys. Lett. 69 (1996) 3173–3175. https://doi.org/10.1063/1.117951.

[71] Á. Révész, T. Ungár, A. Borbély, J. Lendvai, Dislocations and grain size in ball-milled iron powder, Nanostructured Mater. 7 (1996) 779–788. https://doi.org/10.1016/S0965-9773(96)00048-7.

[72] A. Borbély, The modified Williamson-Hall plot and dislocation density evaluation from diffraction peaks, Scr. Mater. 217 (2022). https://doi.org/10.1016/j.scriptamat.2022.114768.

[73] T. Ungar, G. Tichy, The effect of dislocation contrast on X-ray line profiles in untextured polycrystals, Phys. Status Solidi. 425 (1999) 425–434.

[74] T. Ungár, I. Dragomir, Á. Révész, A. Borbély, The contrast factors of dislocations in cubic crystals: The dislocation model of strain anisotropy in practice, J. Appl. Crystallogr. 32 (1999) 992–1002. https://doi.org/10.1107/S0021889899009334.

[75] G.K. Williamson, W.H. Hall, X-ray line broadening from filed aluminium and wolfram, Acta Metall. 1 (1953) 22–31. https://doi.org/10.1016/0001-6160(53)90006-6.

[76] Y.J. Yin, J.Q. Sun, J. Guo, X.F. Kan, D.C. Yang, Mechanism of high yield strength and yield ratio of 316 L stainless steel by additive manufacturing, Mater. Sci. Eng. A. 744 (2019) 773–777. https://doi.org/10.1016/j.msea.2018.12.092.

[77] H. Chen, T. Lu, Y. Wang, Y. Liu, T. Shi, K.G. Prashanth, K. Kosiba, Laser additive manufacturing of nano-TiC particles reinforced CoCrFeMnNi high-entropy alloy matrix composites with high strength and ductility, Mater. Sci. Eng. A. 833 (2022) 142512. https://doi.org/10.1016/j.msea.2021.142512.

[78] L. Lilensten, J.P. Couzinié, L. Perrière, A. Hocini, C. Keller, G. Dirras, I. Guillot, Study of a bcc multi-principal element alloy: Tensile and simple shear properties and underlying deformation mechanisms, Acta Mater. 142 (2018) 131–141. https://doi.org/10.1016/j.actamat.2017.09.062.

[79] R.L. Fleischer, Solution hardening by tetragonal dist ortions: Application to irradiation hardening in F.C.C. crystals, Acta Metall. 10 (1962) 835–842. https://doi.org/10.1016/0001-6160(62)90098-6.

[80] D. Cui, Y. Zhang, L. Liu, Y. Li, L. Wang, Z. Wang, J. Li, J. Wang, F. He, Oxygen-assisted spinodal structure achieves 1.5 GPa yield strength in a ductile refractory high-entropy alloy, J. Mater. Sci. Technol. 157 (2023) 11–20. https://doi.org/10.1016/j.jmst.2023.01.038.

[81] P. Agrawal, S. Karthikeyan, Enhancement in Strain Hardening on Boron Addition in As-Cast Ti–6Al–4V Alloy, Trans. Indian Inst. Met. 68 (2015) 195–205. https://doi.org/10.1007/s12666-015-0560-6.

[82] V. Gerold, H.P. Karnthaler, On the origin of planar slip in f.c.c. alloys, Acta Metall. 37 (1989) 2177–2183. https://doi.org/10.1016/0001-6160(89)90143-0.

[83] J.P. Couzinié, L. Lilensten, Y. Champion, G. Dirras, L. Perrière, I. Guillot, On the room temperature deformation mechanisms of a TiZrHfNbTa refractory high-entropy alloy, Mater. Sci. Eng. A. 645 (2015) 255–263. https://doi.org/10.1016/j.msea.2015.08.024.

[84] J.T. Fong, Fatigue mechanisms, ASTM International, 1979.

[85] S.I. Rao, C. Varvenne, C. Woodward, T.A. Parthasarathy, D. Miracle, O.N. Senkov, W.A. Curtin, Atomistic simulations of dislocations in a model BCC multicomponent concentrated solid solution alloy, Acta Mater. 125 (2017) 311–320. https://doi.org/10.1016/j.actamat.2016.12.011.